NASA Public Access
Author manuscript
Geochim Cosmochim Acta. Author manuscript; available in PMC 2020 December 02.

Published in final edited form as:
Geochim Cosmochim Acta. 2020 November 1; 288: 36–50. doi:10.1016/j.gca.2020.07.036.

Genetics, Age and Crystallization History of Group IIC Iron Meteorites

Hope A. Tornabene[a], **Connor D. Hilton**[a], **Katherine R. Bermingham**[a,*], **Richard D. Ash**[a], **Richard J. Walker**[a]

[a]Department of Geology, University of Maryland, College Park, Maryland, 20742, USA

Abstract

The eight iron meteorites currently classified as belonging to the IIC group were characterized with respect to the compositions of 21 siderophile elements. Several of these meteorites were also characterized for mass independent isotopic compositions of Mo, Ru and W. Chemical and isotopic data for one, Wiley, indicate that it is not a IIC iron meteorite and should be reclassified as ungrouped. The remaining seven IIC iron meteorites exhibit broadly similar bulk chemical and isotopic characteristics, consistent with an origin from a common parent body. Variations in highly siderophile element (HSE) abundances among the members of the group can be well accounted for by a fractional crystallization model with all the meteorites crystallizing between ~10 and ~26% of the original melt, assuming initial S and P concentrations of 8 wt.% and 2 wt.%, respectively. Abundances of HSE estimated for the parental melt suggest a composition with chondritic relative abundances of HSE ~6 times higher than in bulk carbonaceous chondrites, consistent with the IIC irons sampling a parent body core comprising ~17% of the mass of the body.

Radiogenic ^{182}W abundances of two group IIC irons, corrected for a nucleosynthetic component, indicate a metal-silicate segregation age of 3.2 ± 0.5 Myr subsequent to the formation of Calcium-Aluminum-rich Inclusions (CAI). When this age is coupled with thermal modeling, and assumptions about the Hf/W of precursor materials, a parent body accretion age of 1.4 ± 0.5 Myr (post-CAI) is obtained.

The IIC irons and Wiley have ^{100}Ru mass independent "genetic" isotopic compositions that are identical to other irons with so-called carbonaceous chondrite (CC) type genetic affinities, but enrichments in ^{94,95,97}Mo and ^{183}W that indicate greater *s*-process deficits relative to most known CC iron meteorites. If the IIC irons and Wiley are of the CC type, this indicates variable *s*-process deficits within the CC reservoir, similar to the *s*-process variability within the NC reservoir observed for iron meteorites. Nucleosynthetic models indicate that Mo and ^{183}W *s*-process variability should correlate with Ru isotopic variability, which is not observed. This may indicate the IIC irons and Wiley experienced selective thermal processing of nucleosynthetic carriers, or are genetically distinct from the CC and NC precursor materials.

(hopet@umd.edu).
*Present Address: Department of Earth and Planetary Sciences, Rutgers University, Piscataway, New Jersey, 08854 USA

NASA Author Manuscript
NASA Author Manuscript
NASA Author Manuscript

NASA Author Manuscript NASA Author Manuscript NASA Author Manuscript

Keywords

Group IIC iron meteorites; Highly siderophile elements; Re-Os isotopes; Fractional crystallization; Hf-W chronometry; Accretion age; Genetics; Nucleosynthesis

1. Introduction

Members of magmatic iron meteorite groups are presumed to sample planetesimal cores, with members of each group chemically related through common physical processes, such as fractional crystallization and solid-liquid metal mixing (e.g., Schaudy et al., 1972; Scott and Wasson, 1975; Pernicka and Wasson, 1987). Group IIC meteorites comprise a magmatic iron group with chemical compositions characterized by minor depletions in some volatile siderophile elements, such as Ga and Ge. They are structurally classified as plessitic octahedrites. Based on similar Ni, Ir and Ge concentrations, eight meteorites are currently classified as group IIC magmatic irons (Wasson, 1969; *Meteoritical Bulletin,* 2020).

In addition to chemical similarities, members of a magmatic group should also be characterized by the same nucleosynthetic isotope compositions, given that they are presumed to have crystallized from the same melt. Nucleosynthetic, or "genetic," isotope anomalies in bulk planetary materials are defined by mass independent variations in certain isotope ratios that differ from those estimated for the bulk silicate Earth. The variations are consistent with nucleosynthetic theory and direct isotopic measurements of presolar grains found in primitive meteorites (Arlandini et al., 1999; Burkhardt et al., 2011). The nucleosynthetic anomalies present in bulk planetary materials likely developed by heterogeneous accretion of presolar components to parent bodies. This could result from condensation or evaporation effects, location within the nebula, timing, or any combination of these (e.g., Trinquier et al., 2007; Trinquier et al., 2009; Warren, 2011).

Variations in genetic isotopic characteristics have been used to subdivide meteorites into "carbonaceous chondrite" (CC) and "non-carbonaceous" (NC) types (Warren, 2011). It has been postulated that CC and NC type meteorites formed in discrete feeding zones outboard and inboard of the proto-Jupiter, respectively, and possibly at different times (Warren, 2011; Kruijer et al., 2017; Nanne et al., 2019). For iron meteorites, the excess of *r*-, and potentially *p*-process isotopes of the siderophile element Mo are especially useful for distinguishing CC from NC parent bodies (e.g., Budde et al., 2016; Poole et al., 2017; Worsham et al., 2017, 2019). Based on Mo isotopes, Kruijer et al. (2017) and Poole et al. (2017) concluded that the IIC group is of the CC type.

The ^{182}Hf-^{182}W system ($t_{1/2}$ = 9 Myr; Vockenhuber et al., 2004) can be used to assess the thermal evolution of magmatic iron meteorite parent bodies with respect to both the timing of metal-silicate segregation (i.e., core formation), and the accretion age of the parent body. Model accretion ages are obtained by combining the model segregation ages with thermal models and assumptions about the size, ^{26}Al content, and Hf/W of precursor materials and the parent body (e.g. Kruijer et al. 2017; Hilton et al. 2019). The NC type groups have model accretion ages ranging from 0.3 ± 0.3 to 1.0 ± 0.5 Myr after calcium aluminum rich inclusion (CAI) formation while the CC type groups, on average, have relatively younger

NASA Author Manuscript NASA Author Manuscript NASA Author Manuscript

model accretion ages of 1.1 ± 0.6 to 1.4 ± 0.5 Myr after CAI formation (Kruijer et al., 2017; Hilton et al., 2019). It has recently been suggested, however, that Hf/W in at least some NC bodies may have been less than in CC parent bodies (Hellmann et al., 2019). If so, this could mean that model accretion ages for some NC bodies are more similar to, or even younger than model accretion ages for CC bodies.

The objectives of this study are to further investigate the chemical and genetic characteristics of the IIC group, assess if any/all meteorites comprising the group can be related by a crystal-liquid fractionation model, further constrain timing of metal-silicate segregation and parent body accretion, and model the chemical characteristics of the parent body.

2. Samples

Five meteorite samples were obtained from the Smithsonian Institution National Museum of Natural History: Ballinoo (USNM 3284), Kumerina (USNM 5711), Perryville (USNM 428), Salt River (USNM 1131) and Wiley (USNM 1328). Cratheús (1950) and the IVA iron meteorite Pará de Minas were obtained from the Museu Nacional/UFRJ, Brazil. Unter Mässing (MPK 3074A) was obtained from Senckenberg Forschungsinstitut und Naturmuseum, Germany. Darinskoe was obtained from the Geological Museum of the Geological and Geophysical Institute of the Siberian Branch, Russia. A meteorite identified as Cratheús (1950) (ME 2712) was obtained from the Field Museum (Chicago).

3. Analytical Methods

3.1. Laser Ablation ICP-MS

The ten samples were cut into 0.03–0.13 g pieces using a diamond blade saw with high purity water as a coolant and lubricant. The cut samples were polished with carborundum paper until one flat surface was free of diamond blade markings. To remove any contamination from the blade and carborundum paper, each sample was ultrasonicated in ethanol for approximately one minute after preparation. Siderophile element concentrations were obtained for polished surfaces by laser ablation using a *New Wave* UP213 ultraviolet laser coupled to a *Thermo-Finnigan Element 2* inductively coupled plasma mass spectrometer (ICP-MS). Laser ablation was achieved with a repetition rate of 7 Hz and laser output was varied to maintain an energy flux of ~2–4 Jcm^{-2}. All data were processed using *LAMTRACE* (Rusk, 2009) using known concentrations of reference materials (iron meteorites Hoba and Filomena). Initially, Fe was used as an internal standard for the IIC group using accepted values in the literature (Buchwald, 1975; Wasson, 1969), then all concentrations were recalculated to force Fe, Ni, and Co concentrations to sum to 100%.

3.2. ^{187}Re-^{187}Os and siderophile element analysis

Bulk sample isotope dilution measurements of the highly siderophile elements (HSE) Re, Os, Ir, Ru, Pt and Pd were performed on ~50–100 mg pieces of polished chips using combined multi-collector ICP-MS and thermal ionization mass spectrometry (TIMS). The chemical-separation techniques used have been previously described (e.g., Walker et al., 2008). In brief, appropriate amounts of separate ^{185}Re-^{190}Os and ^{191}Ir-^{99}Ru-^{194}Pt-^{105}Pd mixed spikes were added to each sample. Each mixture (sample and spike) was sealed and

NASA Author Manuscript NASA Author Manuscript NASA Author Manuscript

digested in *Pyrex™* Carius tubes along with 5 mL of high purity concentrated HNO_3 and 2.5 mL of high purity concentrated HCl. The tubes were then heated to approximately 230°C for ≥24 hours. After heating, Os was separated using a carbon tetrachloride solvent extraction method (Cohen and Waters, 1996) and further purified by microdistillation (Birck et al., 1997). The Os total processing blank was 2 ± 1 pg (n = 3), which was negligible relative to the quantities of Os extracted from the samples. Approximately 80–200 ng of purified Os were loaded onto an outgassed Pt filament along with Ba hydroxide activator and analyzed as OsO_3^- by a *Thermo Fisher Triton* TIMS using standard techniques. Osmium isotope dilution data were corrected for natural and instrumental mass fractionation by normalizing $^{190}Os/^{188}Os$ to 3.08271 (Allègre and Luck, 1980).

Rhenium and the remaining HSE were dissolved in low molarity hydrochloric acid, and extracted and separated using anion exchange columns (Rehkämper and Halliday, 1997). Each sample was loaded into a column with 1 M HCl, then Re and Ru were eluted with 12 mL 6 M HNO_3, Ir and Pt were eluted with12 mL concentrated HNO_3 and Pd was eluted with 15 mL concentrated HCl. The aliquots of Re and Ru were then dried and re-dissolved in 1 M HCl and loaded onto a smaller anion column for further purification. The Re, Ir, Ru, Pt and Pd blanks for this procedure averaged 4 ± 2, 5 ± 7, 40 ± 10, 40 ± 4 and 100 ± 100 pg, respectively (n = 3). All analyses were blank corrected but the corrections had negligible impact on analytical uncertainties. Rhenium, Ru, Ir, Pt and Pd were analyzed using a *Thermo Neptune Plus* multi-collector ICP-MS. Tungsten was added to Re solutions to correct for mass fractionation. Estimated uncertainties for Re and Os are ~0.1%. Uncertainties for other HSE are better than 1%.

High precision measurements of Os, Mo, Ru and W isotopic compositions were achieved by dissolving approximately 2–4 g pieces of the meteorites in ~50 mL 8 M HCl at 130 °C for at least 48 hours in Teflon® beakers. The resulting solution was centrifuged and the supernatant was separated into four aliquots to be separately processed for Os, Mo, Ru and W isotopic measurements. Osmium isotopic analysis for cosmic ray exposure (CRE) effects were accomplished by the same chemical separation and purification techniques as discussed above for Os analysis by isotope dilution. Approximately 100–300 ng Os was loaded onto outgassed Pt filaments, covered with Ba hydroxide, and analyzed as OsO_3^- using a *Thermo Fisher Triton* TIMS and standard techniques (e.g., Walker, 2012). Osmium isotopic data were corrected for natural and instrumental mass fractionation by normalizing $^{190}Os/^{188}Os$ to 3.08271 (Allègre and Luck, 1980).

All isotopic compositions in this study are reported using the μ notation, which corresponds to the deviation in parts per million of an isotopic ratio of a sample relative to the ratio measured in a laboratory standard (e.g., Os):

$$\mu^{189}Os = \left(\frac{\frac{189}{188}Os_{sample}}{\frac{189}{188}Os_{standard}} - 1 \right) * 10^6 \qquad \text{Eq. 1:}$$

During the course of measurements for this study, the external (2σ) reproducibility of repeated analyses of the laboratory Os standard was ± 8 ppm for $\mu^{189}Os$ (n=9).

NASA Author Manuscript

NASA Author Manuscript

NASA Author Manuscript

The chemical separation and purification techniques for Mo have been described in Worsham et al. (2016). Aliquots of Mo were dissolved in 1 M HF, loaded onto an anion column with ~1.4 mL AG 1 × 8 200–400 mesh resin, and eluted with 6 M HNO_3 – 3 M HF. Then, the samples were dried, dissolved in 6 M HCl, loaded onto a smaller anion column with ~0.3 mL AG 1×8 200–400 mesh resin and eluted with 1 M HCl. This smaller anion column elution was repeated twice. The Mo aliquots were dried, re-dissolved in 6 M HCl and approximately 500–1000 ng Mo were loaded onto outgassed Re filaments along with ~2 μL of 5 μg/μL $La(NO_3)_3$ activator solution. The Mo blank for this procedure was <1 ng. A double filament assembly was used with the same amount of $La(NO_3)_3$ activator on the second filament. Molybdenum was analyzed as MoO_3^- by a *Thermo Fisher Triton Plus* TIMS using data acquisition and reduction methods detailed in Worsham et al. (2016). To correct for O interferences, the $^{100}Mo^{18}O^{16}O_2^-$ species was measured using a 10^{13} Ω resistor-equipped amplifier. Molybdenum isotopic data were corrected for natural and instrumental mass fractionation by normalizing $^{98}Mo/^{96}Mo$ to 1.453171 (Lu and Masuda, 1994). The external (2σ) reproducibility of repeated analyses of the laboratory standard analyzed were ± 17 ppm, ± 15 ppm, and ± 8 ppm for $\mu^{94}Mo$, $\mu^{95}Mo$, and $\mu^{97}Mo$, respectively (n=8).

The chemical separation and purification techniques for Ru have been described in Bermingham et al. (2016). Ruthenium aliquots were dissolved in 0.15 M HCl, loaded onto a primary cation column with ~10 mL AG50WX8 200–400 mesh resin and eluted with 0.15 M HCl. The aliquots were then dried, dissolved in 1 M HCl, and loaded onto a secondary anion column with ~3.8 mL AG 1 × 8 200–400 mesh resin and eluted with 8 M HNO_3 and concentrated HNO_3. Ruthenium was then further purified by microdistillation. The Ru blank for this procedure was <10 pg. Approximately 800–1000 ng Ru were loaded onto outgassed Pt filaments along with barium hydroxide activator and analyzed as RuO_3^- by a *Thermo Fisher Triton Plus* TIMS using data acquisition and reduction methods detailed in Bermingham et al. (2016). The Ru isotopic data were corrected for natural and instrumental mass fractionation by normalizing $^{99}Ru/^{101}Ru$ to 0.745075 (Chen et al., 2010). The external (2σ) reproducibility of repeated analyses of the laboratory standard analyzed was ± 7 ppm for $\mu^{100}Ru$ (n=7).

After drying the 8 M HCl W aliquot, it was re-dissolved in 0.5 M HCl – 0.5 M HF, eluted through an anion column packed with AG 1×8 100–200 mesh resin with 6 M HCl – 1 M HF. This step was repeated three times, each time using progressively less resin and acid (Touboul and Walker, 2012). The W blank for this procedure was <1 ng. The purified W aliquots were dried, dissolved in 1 M HCl – 0.01 M HF and approximately 500–1000 ng W were loaded onto an outgassed single Re filament with 1 μL of 5 μg/μL La-5 μg/μL Gd activator solution and analyzed as WO_3^- by a *Thermo Fisher Triton* TIMS using data acquisition and reduction methods detailed in Archer et al. (2017). Mass interferences from ReO_3^- were monitored and corrected. Tungsten isotopic data were corrected for natural and instrumental mass fractionation by normalizing $^{186}W/^{184}W$ to 0.92767 (Völkening et al., 1991). The external (2σ) reproducibility of repeated analyses of the laboratory standard analyzed were ± 5 ppm and ± 6 ppm for $\mu^{182}W$ and $\mu^{183}W$, respectively (n=7).

NASA Author Manuscript NASA Author Manuscript NASA Author Manuscript

3.3. Cosmic ray exposure corrections

Cosmic ray exposure can modify the isotopic composition of Mo, Ru, and W of iron meteorites (Fischer-Godde et al., 2015; Worsham et al., 2017; Bermingham et al., 2018). The magnitude of the cosmogenic effects depends on the location of the sample within the meteoroid and the duration of CRE (Fischer-Godde et al., 2015). Osmium nuclides dominated by *s*- and *r*-process (e.g., ^{189}Os and ^{190}Os) were homogeneously distributed and mixed in the solar protoplanetary disk (Walker, 2012). Consequently, Os isotopes do not show nucleosynthetic variations among iron meteorites. Osmium-189 is used as a sensitive monitor for neutron fluence in iron meteorites due to the predictable way Os isotopes are affected by CRE and because of its comparatively large neutron cross section and thermal resonance integral (Walker, 2012). Based on the analytical uncertainty for the measured ^{189}Os/^{188}Os, it is assumed that the sampled portions of the meteorites with μ^{189}Os values within ± 8 ppm of 0 were minimally affected by CRE.

4. Results

4.1. Composition analysis by laser ablation ICP-MS

The IIC irons are plessitic octahedrites with kamacite spindle widths of only ~60–70 μm. Therefore, averaging accumulated data obtained from multiple ~5 mm long laser ablation tracks are generally interpreted to be representative of the composition of the interrogated polished surface. Average elemental concentrations obtained by LA-ICP-MS and 2σ variations for multiple lines of analysis for each meteorite are given in Table 1. During laser ablation analysis, however, it was noted that phosphide veins were visible in all samples. Siderophile elements are generally in very low abundances in phosphides compared to average metal, so the siderophile element concentrations averaged along an ablation track that intersected a phosphide vein tended to be lower than tracks that did not intersect a phosphide vein. The siderophile element data obtained for the phosphide veins were not subtracted from the averages. This accounts for some of the absolute abundance heterogeneity observed when comparing data for multiple lines, rather than reflecting heterogeneities in the metal. The concentrations of Ir, Ga, and Ge determined by laser ablation are within 30%, and Ni concentrations are within 10% of the concentrations reported by Wasson (1969).

Bulk composition data, normalized to CI chondrites, are characterized by broadly similar patterns for most IIC irons (Fig. 1). Consistent with their group II classification, there is a slight depletion in volatile siderophile elements, such as Ga and Ge, relative to the more refractory siderophile elements, such as W and Re. Patterns are also characterized by major depletions in the multivalent elements V, Cr, P and Zn.

Of note, the siderophile element abundance pattern for Wiley is quite different from that of the other IIC irons. Also, the data we acquired for the Cratheús (1950) sample obtained from the Field Museum did not match the literature values for Cratheús (1950), as reported by Buchwald (1975) and Wasson (1969), or our data for the Cratheús (1950) sample obtained from Museu Nacional, Brazil. Instead, it has a composition that matches literature data for Cratheús (1931), a group IVA iron meteorite (Buchwald, 1975). Of further note, the

NASA Author Manuscript

NASA Author Manuscript

NASA Author Manuscript

Cratheús (1950) specimen from the Field Museum and the Pará de Minas specimen from the Museu Nacional, Brazil have siderophile element abundances that are nearly identical for most siderophile elements (Fig. 1). Pará de Minas is a group IVA iron.

4.2. Highly siderophile element concentrations

The HSE concentration data for bulk samples obtained by isotope dilution are presented in Table 2. The concentrations of Re, Ru and Pd obtained by isotope dilutions are all within 30%, and Os, Ir and Pt concentrations are all within 20% of the concentrations obtained by LA-ICP-MS. Chondrite normalized data for most of the meteorites form nested patterns that do not cross with the patterns of other IIC irons. The HSE abundance patterns for the IIC irons, proceeding from lower to higher Ni, and excluding Wiley, are characterized by decreasing abundances of Re, Os, Ir, Ru, and Pt, with little change in Pd (Fig. 2). Consistent with the LA-ICP-MS data, the isotope dilution HSE patterns for Cratheús (1931) from the Field Museum and Pará de Minas are essentially identical (Table 2; Fig. 2). Thus, we conclude that the Field Museum Cratheús (1931) is likely mislabeled as Cratheús (1950). We also infer that Cratheús (1931) and Pará de Minas are the same meteorite.

Wiley has similar Ir, Ga, Ge, and Ni concentrations to the other IIC irons which explains its classification as a IIC iron. Yet, as noted from the LA-ICP-MS data, the bulk HSE pattern shape for Wiley strongly diverges from the other IIC irons (Fig. 2). Although the Re and Os concentrations of Wiley could be accounted for as a result of extensive crystal-liquid fraction from a melt that generated the other IIC irons, its Ir, Ru and Pt abundances are not consistent with this type of model. Our chemical results strongly suggest that Wiley is not a IIC iron and is unlikely to have formed from the same parental melt as the other IIC irons. It should henceforth be classified as ungrouped. The isotopic data presented below are consistent with prior studies (e.g., Worsham et al., 2019) that have also arrived at this conclusion.

4.3. Re-Os systematics

The Re-Os isotopic data for IIC irons are provided in Table 2. Duplicate isotope dilution analyses of Darinskoe differ from each other beyond analytical uncertainties and plot slightly below the IIC isochron, indicative of post-crystallization Re gain or Os loss (Fig. 3). The Darinskoe data likely reflect minor (1–2%), recent open-system behavior of Re-Os, possibly occurring on Earth.

The IIC irons are characterized by a limited range in $^{187}Re/^{188}Os$ from 0.3637 to 0.4875 and $^{187}Os/^{188}Os$ from 0.1242 to 0.1339. Precision of the resulting isochron slope is consequently limited, with a regression of $^{187}Re/^{188}Os$ versus $^{187}Os/^{188}Os$ data for seven IIC irons (excluding Darinskoe) giving an initial $^{187}Os/^{188}Os = 0.0956 \pm 0.0010$ and an age of 4538 ± 140 Myr, calculated using *ISOPLOT* (Ludwig, 2003). Nevertheless, except for Darinskoe, all IIC irons plot within uncertainties of a 4.56 Ga reference isochron, indicating closed-system behavior for these samples (Fig. 3).

4.4. Osmium isotopic compositions

The mass independent isotopic compositions of Os and Pt have been shown to be viable dosimeters of neutron capture effects resulting from long-term CRE (Fischer-Gödde et al.,

NASA Author Manuscript NASA Author Manuscript NASA Author Manuscript

2015). Osmium isotopic compositions for the IIC irons analyzed (Ballinoo, Darinskoe and Perryville) and Wiley are presented in Table 3. All have μ^{189}Os values ranging from −5 ± 7 to 5 ± 5, hence, no resolved variations from standards. Consequently, Mo, Ru and W isotopic data are not corrected for CRE.

4.5. Molybdenum, Ru and W isotopic compositions

Molybdenum, Ru and W isotopic compositions for Ballinoo, Darinskoe, Perryville and Wiley are reported in Tables 4–5. The $\mu^{94,95,97}$ Mo and μ^{183}W values for the averages of Ballinoo, Darinskoe and Perryville are offset to values that are higher than all other CC type iron meteorites reported by Kruijer et al. (2017), Poole et al. (2017), Bermingham et al. (2018) and Worsham et al. (2019). The new Mo isotopic data are broadly consistent with the averages reported by Kruijer et al. (2017), Poole et al. (2017), and Worsham et al, (2019) for IIC irons and Wiley (Table S1). The $\mu^{94,95,97}$ Mo and μ^{183}W values for Wiley are even higher than for the *bona fide* IIC irons. Average μ^{183}W values for Ballinoo and Perryville are +28 ± 3 (2SE), consistent with the +30 ± 4 value reported for Ballinoo and Kumerina by Kruijer et al. (2017). The average μ^{183}W value for Wiley is +44 ± 7, which overlaps within uncertainty with the +52 ± 3 value reported by Kruijer et al. (2017). All of the *bona fide* IIC irons analyzed for μ^{100}Ru are characterized by identical isotopic compositions, within uncertainties, averaging −99 ± 2 (2SE). This value is consistent with the −104 ± 5 average value reported for Kumerina, Perryville, and Unter Mässing by Worsham et al. (2019), and with all other CC type irons reported by Fischer-Gödde et al. (2015), Bermingham et al. (2018) and Worsham et al. (2019). The average μ^{100}Ru for Wiley is −106 ± 8, which is in agreement with the −107 ± 8 value reported by Worsham et al. (2019).

5. Discussion

5.1. Crystallization models

Due to the predictable behavior of the HSE during magmatic processes, modeling of the HSE has proven useful in constraining the nature of the crystallization process of parent body cores (Pernicka and Wasson, 1987; Chabot and Jones, 2003; McCoy et al., 2011). Modeling HSE behavior for the IIC group can provide insight into the compositional evolution of the IIC parent body as well as the contributions of liquid-solid metal mixing during the crystallization process.

The HSE patterns of the group IIC irons are qualitatively consistent with fractional crystallization in that concentrations of Re, Os, Ir, Ru, and Pt, normally characterized by solid metal-liquid metal D values >1 (where D values are solid/liquid concentration ratios), decrease in metal as crystallization proceeds, while Pd (normally characterized by solid metal-liquid metal D values <1), increases. In this study, appropriate solid metal-liquid metal D values for the HSE were calculated using the parameterization method developed by Jones and Malvin, (1990) and advanced by Chabot et al. (2017). A comprehensive description of this method is described in the supplementary materials.

The concentrations of P and particularly S in a metallic melt can strongly affect the solid-metal liquid-metal D values of HSE during crystallization of the melts (e.g., Chabot et al.,

NASA Author Manuscript NASA Author Manuscript NASA Author Manuscript

2017). Increasing concentrations of S and P reduce the tendency of the liquid metal to host most HSE and moderately siderophile elements (MSE). Initial S and P and subsequent change in concentration must, therefore, be estimated for successful modeling of metal crystallization. However, S and P are highly incompatible elements with solid metal. As a result, they remain concentrated in the melt during fractional crystallization and leave limited direct traces of their melt concentrations in the resulting solids. Consequently, the variables for our model include the S, P and HSE compositions of the initial melt from which the IIC irons crystallized.

As has been done for other iron meteorite groups (Hilton et al., 2019), we constrain the initial P content by dividing the average P composition of the least evolved iron meteorite in the IIC suite, Darinskoe (~0.3 wt.%) by the constant D_o value (where D_o is the solid metal-liquid metal D value in the light-element-free Fe-Ni system) for P (0.1) (Chabot et al., 2017). This suggests an initial P content of approximately 3 wt.%. An initial bulk S content can be estimated from the Ir, Ga and Ge versus Au trends (Wasson, 1999; Chabot, 2004; Goldstein et al., 2009). Gallium, Ge and Au partition are sensitive to bulk S concentrations and produce distinct non-linear trends. Thus, these elements serve as good proxies to constrain initial S. However, fractional crystallization models cannot account for Ga, Ge and Au with a single initial S content. The Ga and Ge trends are best fit by ~9 ± 1 wt.% initial S, while the Ir trend is best fit by ~0 wt.% initial S (Fig. S1). Due to the presence of abundant (~0.3 wt.% S) troilite nodules in some IIC irons (Buchwald, 1975), it is unlikely the IIC body had low initial S. This conclusion is supported by the fact that the IIC group is not strongly depleted in other volatile siderophile elements (Fig. 1). Nevertheless, in order to better constrain initial S, we model HSE evolution with both relatively high and low initial S concentrations.

Meteorites that formed by fractional crystallization of a metallic core can represent solids directly precipitated from a liquid that they were in equilibrium with, equilibrium melt trapped in and mixed with solids, or a liquid composition preserved by entrapments in earlier formed solids (Wasson, 1999; Walker et al., 2008). In chemical evolution models, a liquid track represents the path of evolving liquid concentrations resulting from fractional crystallization. The accompanying solid track represents the path of the concentrations of equilibrium solids precipitating from the evolving liquid. A meteorite with a concentration that plots along the solid or liquid tracks can be interpreted as representing an equilibrium solid or liquid, respectively. A meteorite with compositions that plots between the tracks may represent a mixture of equilibrium solids and trapped coexisting liquids.

Our detailed modeling of fractional crystallization of the IIC system begins with Re and Os, as they are the best measured HSE, and because we assume their initial concentration ratio was within the chondritic range (~0.39–0.44; Walker et al., 2002). Initial Re concentrations were estimated assuming that the first crystallizing solids had a Re concentration similar to that of the least evolved meteorite, Darinskoe. Osmium concentrations were constrained by iteration, assuming the $^{187}Re/^{188}Os$ in the initial melt was similar to chondrites. The concentrations of the rest of the HSE were constrained by varying initial concentrations to match those of Darinskoe. As noted above, although the Re-Os isotopic data for Darinskoe do not plot within uncertainties of a 4.56 Ga reference isochron, the offsets from the

NASA Author Manuscript NASA Author Manuscript NASA Author Manuscript

isochron suggest gain or loss of only 1–2% of the concentrations of Re and Os. Such minimal open-system behavior should not affect the modeling.

Model solid and liquid evolution tracks of Re concentration versus Re/Os with IIC data are shown in Figure 4a–b. Two contrasting models, A and B, defined by 0 and 8 wt.% initial S, and 3 and 2 wt.% initial P, respectively, are considered. Additional models with varying S and P concentrations are presented in the supplemental materials. In both models A and B, Darinskoe is assumed to represent an equilibrium solid that formed following ~10% fractional crystallization. Since Cratheús (1950), Ballinoo, Perryville, Kumerina, and Unter Mässing plot outside of the liquid and solid tracks, model A is inconsistent with the IIC pattern. By contrast, all IIC irons plot between solid and liquid tracks, and can therefore be accounted for in model B. We conclude that the S and P content of model B best match the HSE concentration variations in the group.

Given model B initial parameters, Darinskoe and Unter Mässing plot along the solid track representing equilibrium solids at 10 and 26% fractional crystallization. The modeling of the other HSE, using these initial parameters (Fig. S3), are in good agreement with observed concentrations of HSE (Fig. 5a–b), with details provided in the supplemental materials. For this model, the HSE compositions of most IIC irons reflect variable degrees of fractional crystallization, accompanied by melt trapping or mixing from the chemical evolution path. The similar HSE concentrations of Cratheús (1950) and Perryville indicate they likely crystallized at about the same point in the crystallization sequence, as is also true for Ballinoo and Kumerina.

The initial melt concentrations of HSE calculated from the preferred Model B for the IIC parent body core are given in Table 6, along with estimated initial HSE concentrations for the magmatic group IVB, IVA, and South Byron Trio (SBT) irons for comparison (Walker et al., 2008; McCoy et al., 2011; Hilton et al., 2019). Results are shown in Figure 6 along with a pattern representative of average carbonaceous chondrites (Horan et al., 2003). The estimated HSE composition of the parent core for model B is approximately six times higher than the carbonaceous chondrite average. If all HSE were extracted from the silicate shell of the body into the core, these projected concentrations suggest the core was ~17% the mass of the IIC parent body.

5.2 Hf-W Chronology of Core Formation and Parent Body Accretion

The IIC irons can be successfully modeled by fractional crystallization from the same parental melt and thus likely reflect derivation from a single parent body core. As such, the W isotopic composition of the IIC irons can be used to constrain timing of core formation. Tungsten-182 depletions in iron meteorites have been previously used to determine the timing of parent body core formation, assuming an instantaneous core formation event (e.g., Kruijer et al., 2017). The average μ^{182}W value for the IIC body is −274 ± 8, with a μ^{182}W value corrected for excess ^{183}W of −314 ± 9 (Fig. 7; see supplementary materials for details). Metal-silicate Hf-W model ages are calculated relative to a solar system initial value of −349 ± 7 obtained from CAI (Kruijer et al., 2014a) and assuming a present day chondritic μ^{182}W value of −191 ± 8 (Kleine et al., 2004). The corrected value corresponds to a model metal-silicate differentiation age of 3.2 ± 0.7 Myr after CAI formation. This model

NASA Author Manuscript

NASA Author Manuscript

NASA Author Manuscript

differentiation age overlaps, within uncertainty, all CC type body model differentiation ages reported to date, but is the only iron meteorite group that is resolved from all NC type body model differentiation ages (Kruijer et al., 2017; Hilton et al., 2019).

The timing of core segregation can be used to assess the accretion times of meteorite parent bodies by modeling the thermal evolution of bodies heated by the decay of ^{26}Al. This model requires the knowledge of the temperature at which metal segregation and melting occurred and is dependent on the initial S concentration of iron meteorite parent bodies (Kruijer et al. 2014b). As has been done for other CC type parent bodies, an accretion age is calculated for the IIC parent body assuming single-stage core formation at a given temperature. Using a thermal model described by Kruijer et al. (2017) and Hilton et al. (2019), a parent body accretion age for the IIC group is 1.4 ± 0.5 Myr after CAI formation is obtained (see supplement for details). This age overlaps within uncertainties with all CC and NC type iron meteorite parent bodies, with the exception of the NC type IC group, which is resolved as older (Kruijer et al., 2017; Hilton et al., 2019).

5.3. Parent Body Genetics

Molybdenum, Ru and W isotopic heterogeneities observed in iron meteorites have been attributed to the incorporation of different proportions of materials with distinctive nucleosynthetic signatures (*p-, r-,* and *s*-process nuclides) (e.g., Dauphas et al., 2004). These signatures can be used to assess the genetic relationships among meteorite groups and possible changes in the isotopic composition of the solar nebula with time.

In iron meteorites, Mo is useful as a tracer of the distribution of nucleosynthetic components within the solar nebula. The NC and CC types appear to define two distinct Mo *s*-process mixing lines, most easily observed in a plot of μ^{94}Mo vs. μ^{95}Mo (Budde et al., 2016; Poole et al., 2017; Worsham et al., 2017). The NC type irons show variable Mo isotopic compositions along an *s*-process mixing line (Fig. 8), while most CC irons are indistinguishable within analytical uncertainties (Bermingham et al., 2018) and are characterized by enrichments in *r*-process Mo relative to the NC trend (Fig. 8). Although some carbonaceous chondrites and chondrules exhibit similar Mo isotope anomalies (Burkhardt et al., 2011; Budde et al., 2016), the IIC group exhibits the largest nucleosynthetic ^{94,95,97}Mo isotope anomalies of any iron meteorite group analyzed to date. For example, the μ^{95}Mo value for IIC irons are offset from the average CC μ^{95}Mo value by approximately 50 ppm. Further, Wiley has the largest anomalies yet reported for irons and is offset from the average CC μ^{95}Mo value by approximately 130 ppm. The IIC group and Wiley do not fall within the CC type cluster but instead plot along an apparent *s*-process mixing line with the CC type irons that is generally parallel to the NC trend. This observation led Kruijer et al. (2017) and Poole et al. (2017) to conclude that the IIC group is of the CC type. A linear trend from the CC cluster to the IIC group and Wiley is consistent with a nebular feeding zone characterized by variable *s*-process deficits coupled with *r*- and *p*-process (e.g., μ^{92}Mo) excesses, in constant proportions, relative to NC bodies.

Isotopes of Ru add an additional dimension to examine genetic components in irons. Using a plot of ^{92}Mo vs. ^{100}Ru, Dauphas et al. (2004) noted a linear Mo-Ru relationship between iron meteorite groups and termed it the “Mo-Ru cosmic correlation.” On a similar plot of

NASA Author Manuscript

NASA Author Manuscript

NASA Author Manuscript

μ^{97}Mo vs. ^{100}Ru, the NC type parent bodies are characterized by Mo and Ru with variable *s*- and *r*- process deficits relative to Earth (Fig. 9). By contrast, most of the CC type parent bodies of irons plot within uncertainties of one another, consistent with a nebular feeding zone with homogeneously mixed ^{97}Mo and ^{100}Ru isotopic compositions (Bermingham et al., 2018; Worsham et al., 2019). The IIC irons and Wiley, however, are characterized by μ^{100}Ru values consistent with CC type irons, but greater $\mu^{94,95,97}$Mo values, as noted by Worsham et al. (2019). Consequently, they plot well off the ^{97}Mo-^{100}Ru correlation (Fig. 9; Fig. S5). This is unexpected because in order to generate the linear trend on a plot of μ^{94}Mo vs. μ^{95}Mo defined by CC type irons (Fig. 8), the IIC group and Wiley would have to have incorporated precursor materials with variable *s*-process deficits in constant proportions. Yet the IIC irons and Wiley have no accompanying *s*-process deficits for ^{100}Ru.

Worsham et al. (2019) noted the NC type irons are characterized by correlated variations in μ^{i}Mo and μ^{100}Ru, yet homogeneous μ^{183}W (Fig. 7). Conversely, the CC type irons are characterized by correlated μ^{i}Mo and μ^{183}W, but homogeneous μ^{100}Ru (Fig. 9). To account for this inconsistency, Worsham et al. (2019) concluded that the isotopic homogeneity observed for μ^{183}W in the NC domain, and μ^{100}Ru in the CC domain, could be explained by assuming that each domain was initially homogeneous with respect to the isotopic compositions of all three elements. Isotopic heterogeneity might then have been introduced for some elements as a result of heating, variable volatilization, and partial loss of some elements or their presolar carrier phases. Under the more reducing conditions and higher temperatures commonly envisioned for the NC domain, Worsham et al. (2019) posited that based on 50% condensation temperatures, the extant, reduced species of Mo and Ru would have been more readily volatilized than the high refractory W, preserving ^{183}W isotopic homogeneity, but causing Mo and Ru isotopic heterogeneity. Under the more oxidizing and lower temperature conditions commonly envisioned for the CC domain, Worsham et al. (2019) proposed that Mo and W may have formed oxides more readily than Ru. Given that some oxide species of Mo and W are more volatile than reduced Ru (Fegley and Palme, 1985), this could account for the preservation of Ru isotopic homogeneity, but variable loss of ^{183}W and *s*-process isotopes of Mo. A similar model was proposed by Fischer-Gödde et al. (2015) to retain Ru isotopic homogeneity while generating Mo isotopic heterogeneity among precursor materials for carbonaceous chondrites.

5.4. Chemical evidence for selective volatilization processes affecting Mo, Ru and W

The putative selective volatilization processes, coupled with differences in oxidation states between CC and NC domains to create mass independent isotopic heterogeneity, as proposed by Worsham et al. (2019), might be expected to have left some evidence in the chemical compositions of the parent bodies. For example, if the Mo and W isotopic differences between NC and CC type irons are the result of variable, volatile-related losses of presolar phases bearing Mo and W in the CC domain, relative depletions in Mo and W abundances might accompany the isotopic heterogeneity of these elements in CC irons, compared with NC irons. Given that the IIC irons and Wiley are characterized by the largest Mo and W isotopic anomalies, it is also plausible that the greatest effects of loss would be most evident in these meteorites.

NASA Author Manuscript NASA Author Manuscript NASA Author Manuscript

To assess whether Mo and W were compositionally depleted in IIC irons and Wiley relative to other CC bodies requires knowledge of the initial melt compositions of each parent body core. Although initial melt compositions can be estimated for HSE, as discussed above, the paucity of appropriate D values for other siderophile elements make their estimation more problematic. Nevertheless, during fractional crystallization, concentrations of most siderophile elements generally decrease in later crystallized solids, therefore the least evolved irons from a magmatic iron meteorite group most closely reflect the initial bulk composition of the parent body core. Consequently, we assess the depletions of W and Mo (CI-normalized), relative to other siderophile elements by considering the least chemically evolved CC irons (e.g., highest Re and Os concentrations) of each of the IIC, IVB, South Byron Trio (SBT) groups (Darinskoe, Cape of Good Hope, and Babb's Mill (Troost's Iron), respectively), and an NC iron (Jamestown, IVA group). Depletion factors (X_i*) are calculated using Eq. 2;

$$X_i^* = \left(\frac{X_i}{\frac{[X_o + X_n]}{2}} \right) \quad \text{Eq. 2:}$$

where X_i is the concentration of the specified element for each sample and X_o and X_n are concentrations of Os and Ir, and Ir and Pt used in the calculation for W and Mo, respectively. Osmium, Ir and Pt are chosen for the reference elements because they have 50% condensation temperatures that bracket the temperatures for W and Mo (e.g., Fig. 1). Darinskoe (IIC) and Wiley show no discernible depletions in Mo and W relative to the least evolved irons of other CC groups (SBT and IVB), for which comparable data are available (Fig. 10a–b). Of note, the IVB and SBT groups *are* characterized by depletions of W. Volatility related losses for oxidized species of W and Mo might also be expected to be accompanied by depletions in the moderately volatile siderophile elements, Ga and Ge, yet Darinskoe and Wiley are characterized by comparatively high Ga and Ge abundances, relative to most other CC irons (Fig. S6). The lack of discernable depletions of Mo and W does not exclude the model of Worsham et al. (2019), as the envisioned volatilized presolar components may have comprised only a small fraction of the overall abundances of Mo and W. Nevertheless, the lack of depletions also does not provide "smoking gun" evidence in favor of this type of process.

The next chemical characteristic of NC and CC type meteorites to consider regarding the volatilization model of Worsham et al. (2019) is oxidization state of the parent body and precursor materials. The chemical data recorded in the meteorites are mainly a reflection of oxidation conditions *during* planetesimal differentiation, which is not necessarily directly relatable to nebular conditions during the initial accretionary period, within which the selective volatilization processes presumably acted. Nevertheless, the oxidization states of planetesimals must likely, at least in part, reflect pre-accretionary conditions, and so are worthy of examination.

The oxidation states of various planetesimals at the time of primary differentiation can be broadly compared, based on several chemical criteria including initial Fe/Ni (or Ni content),

NASA Author Manuscript NASA Author Manuscript NASA Author Manuscript

the concentrations of HSE estimated for the initial core melt, as well as the abundances of multivalent, redox sensitive elements such as V relative to other siderophile elements.

The average Fe/Ni (or Ni content) of an iron group is normally assumed to reflect the proportion of Fe incorporated in the silicate shell of a planetesimal relative to the core. Thus, if Fe-Ni abundances were not fractionated in the nebula, it can be presumed that the lower the initial Fe/Ni (or higher the Ni content) of a core, the smaller the relative mass proportion of the core to the mantle. There is not a clear-cut division between NC and CC iron meteorite parent bodies with respect to Ni, although some CC groups, e.g., IVB and SBT, tend toward much higher Ni than the NC groups (Fig. S6). Group IIC irons, however, have approximately the same Ni content as the NC group IVA irons, with similar estimated initial Ni contents of 9.8 and 8.1 wt.%, respectively. This suggest a moderately oxidized parent body compared to, e.g., IIAB (NC) and IIIF (CC) parent bodies, but one that was *less* oxidized than the IVB and SBT parent bodies (also CC bodies).

Wiley has a Ni content of 10.8 wt.% and is characterized by higher Ru, Pt and Pd concentrations relative to the IIC group (Fig. 2). This may indicate a more oxidized parent body relative to the IIC parent body, but as a single, ungrouped iron, a more precise estimation is impossible.

Similarly, core size can also potentially be constrained from the abundances of HSE estimated for the initial core melt. The higher the initial abundance, the proportionally smaller the core must be, assuming the bulk parent body was characterized by chondritic abundances of HSE. Base on this type of comparison, IVB and SBT CC type parent bodies are characterized by higher initial HSE and correspondingly smaller core sizes compared with both the IIC and IVA groups (Fig. 6). These data are qualitatively consistent with the conclusions derived from Ni contents, and the conclusions of Ruben et al. (2018). Although the chemical characteristics of Wiley's parent body core are unknown, the relatively high Ru, Pt and especially Pd concentrations may suggest a similar, or relatively larger core size than the estimated IIC core. Palladium is usually not strongly fractionated in a crystallizing metallic melt, therefore the higher Pd in Wiley relative to the IIC irons suggest that the initial Pd concentration of Wiley's parental melt was modestly higher than that of the IIC initial parental melt. This assumption, in turn, suggests a slightly smaller core for the parent body.

The final indicator of oxidation state of a planetesimal to consider is the magnitude of depletions of multivalent elements, such as V, recorded in the irons. The assumption here is that under more oxidizing conditions, the multivalent elements become less siderophile and increasingly incorporated into the silicate portions of planetesimals. Hence, abundance estimates for parental cores should be increasingly depleted relative to other siderophile elements with increased state of oxidation.

Chondritic proportions of siderophile elements with similar volatilities (i.e. Ir and Rh) provide a good reference frame for relative depletions. For example, calculated V* values (Eq. 2) for the least evolved irons give values of 0.32, 0.07, 0.02, 0.52 and 0.555 for the IVB, SBT, Wiley, IIC, and IVA groups, respectively (Fig. 10c). If these values reflect degree

NASA Author Manuscript NASA Author Manuscript NASA Author Manuscript

of oxidation, then the IIC and the NC type IVA groups formed under similar conditions. Wiley and the least evolved iron of the SBT group are characterized by comparatively lower V* values and likely formed under similar, more oxidizing conditions.

In summary, our results for the IIC parental melt composition indicate a parent body that formed under less oxidizing conditions than some other CC type bodies, such as the SBT and group IVB irons, and similar to some NC parent bodies, such as the IVA group irons (Fig. 6). Although the data for IIC irons do not provide evidence for a more oxidized formational environment compared to other CC type groups, the chemical data for Wiley, particularly its V* value, *do* support a somewhat more oxidized formational environment compared to NC, CC and the IIC irons, albeit the Fe/Ni for Wiley suggests a less oxidizing environment than most other CC irons.

Our new findings do not provide chemical data to support the differential volatility model of Worsham et al. (2019) to account for the genetic isotopic observations involving Ru, Mo and W in NC and CC type irons, as well as IIC irons and Wiley, but also do not invalidate the model. The presumed CC type IIC group and Wiley remain the only known irons that are characterized by combined Mo and ^{183}W isotopic compositions that significantly differ from all other CC types. The enrichments of *p*- and *r*-process isotopes, and depletion of *s*-process isotopes in the IIC group and Wiley, relative to NC and other CC type irons, suggest that the parent bodies of these meteorites originated in a nebular reservoir that was processed in a manner that was distinct from NC and other CC type irons. As noted by Worsham et al. (2019), an alternative possibility to the thermal processing model is that of the existence of a nebular domain with genetic characteristics that differ from NC and CC type meteorites. As the genetic isotope characteristics of additional ungrouped irons become known, our knowledge of the extent of genetic diversity (or lack of additional diversity), in early-formed bodies should expand.

6. Conclusions

1. Siderophile element abundances of IIC iron meteorites are consistent with fractional crystallization between 10 and 26% of the bulk core, assuming a metallic melt containing 8 wt.% initial S and 2 wt.% initial P concentrations. The meteorite Wiley has chemical characteristics inconsistent with IIC irons and should be re-classified as ungrouped.

2. The IIC ^{182}Hf-^{182}W model age of 3.2 ± 0.5 Myr, following CAI formation, indicates a relatively late differentiation age for the parent body compared to NC and most other CC parent bodies. Thermal modeling suggests a parent body accretion age of 1.4 ± 0.5 after CAI formation.

3. Nucleosynthetic Mo, Ru and W isotope compositions indicate the IIC group is isotopically distinct from other known iron meteorite groups. If CC type irons, their Ru compositions support the contention that there was little Ru isotopic heterogeneity in the CC nebular domain. By contrast, Mo and W isotopic data differ from known CC irons. This could reflect differential volatilization of Mo

NASA Author Manuscript NASA Author Manuscript NASA Author Manuscript

and W, relative to Ru in precursor materials, although the chemical data for the IIC irons and Wiley provide little supporting evidence for this.

Supplementary Material

Refer to Web version on PubMed Central for supplementary material.

Acknowledgments

Funding for this work was provided by NASA Emerging Worlds grant NNX16AN07G to RJW. The authors thank the Smithsonian Institution National Museum of Natural History, the Museu Nacional/UFRJ, Brazil, the Senckenberg Forschungsinstitut und Naturmuseum, Germany, the Geological Museum of the Geological and Geophysical Institute of the Siberian Branch, Russia and the Chicago Field Museum for providing us with meteorite samples. Highly helpful feedback was provided by reviewer E.A. Worsham, two anonymous reviewers, as and the AE T. Kleine, who are all thanked for their contributions.

References

Allègre CJ, & Luck JM (1980). Osmium isotopes as petrogenetic and geological tracers. Earth and Planetary Science Letters, 48(1), 148–154.

Archer GJ, Mundl A, Walker RJ, Worsham EA, & Bermingham KR (2017). High-precision analysis of $^{182}W/^{184}W$ and $^{183}W/^{184}W$ by negative thermal ionization mass spectrometry: Per-integration oxide corrections using measured $^{18}O/^{16}O$. International Journal of Mass Spectrometry, 414, 80–86. [PubMed: 30713466]

Arlandini C, Käppeler F, Wisshak K, Gallino R, Lugaro M, Busso M, & Straniero O (1999). Neutron capture in low-mass asymptotic giant branch stars: cross sections and abundance signatures. The Astrophysical Journal, 525(2), 886.

Bermingham KR, Walker RJ, & Worsham EA (2016). Refinement of high precision Ru isotope analysis using negative thermal ionization mass spectrometry. International Journal of Mass Spectrometry, 403, 15–26. [PubMed: 30713465]

Bermingham KR, Worsham EA, & Walker RJ (2018). New insights into Mo and Ru isotope variation in the nebula and terrestrial planet accretionary genetics. Earth and Planetary Science Letters, 487, 221–229. [PubMed: 30880823]

Birck JL, Barman MR, & Capmas F (1997). Re-Os isotopic measurements at the femtomole level in natural samples. Geostandards newsletter, 21(1), 19–27.

Buchwald VF (1975). Handbook of Iron Meteorites. University of California Press, 1418 pp.

Burkhardt C, Kleine T, Oberli F, Pack A, Bourdon B, & Wieler R (2011). Molybdenum isotope anomalies in meteorites: constraints on solar nebula evolution and origin of the Earth. Earth and Planetary Science Letters, 312(3–4), 390–400.

Budde G, Burkhardt C, Brennecka GA, Fischer-Gödde M, Kruijer TS, & Kleine T (2016). Molybdenum isotopic evidence for the origin of chondrules and a distinct genetic heritage of carbonaceous and non-carbonaceous meteorites. Earth and Planetary Science Letters, 454, 293–303.

Chabot NL, & Jones JH (2003). The parameterization of solid metal-liquid metal partitioning of siderophile elements. Meteoritics & Planetary Science, 38(10), 1425–1436.

Chabot NL, Wollack EA, McDonough WF, Ash RD, & Saslow SA (2017). Experimental determination of partitioning in the Fe-Ni system for applications to modeling meteoritic metals. Meteoritics & planetary science, 52(6), 1133–1145. [PubMed: 28943752]

Chen JH, Papanastassiou DA, & Wasserburg GJ (2010). Ruthenium endemic isotope effects in chondrites and differentiated meteorites. Geochimica et Cosmochimica Acta, 74(13), 3851–3862.

Cohen AS, & Waters FG (1996). Separation of osmium from geological materials by solvent extraction for analysis by thermal ionisation mass spectrometry. Analytica Chimica Acta, 332(2–3), 269–275.

Dauphas N, Davis AM, Marty B, & Reisberg L (2004). The cosmic molybdenum–ruthenium isotope correlation. Earth and Planetary Science Letters, 226(3–4), 465–475.

NASA Author Manuscript NASA Author Manuscript NASA Author Manuscript

Fegley B and Palme H (1985) Evidence for oxidizing conditions in the solar nebula from Mo and W depletions in refractory inclusions in carbonaceous chondrites. Earth and Planetary Science Letters 72, 311–326.

Fischer-Gödde M, Becker H, & Wombacher F (2010). Rhodium, gold and other highly siderophile element abundances in chondritic meteorites. Geochimica et Cosmochimica Acta, 74(1), 356–379.

Fischer-Gödde M, Burkhardt C, Kruijer TS, & Kleine T (2015). Ru isotope heterogeneity in the solar protoplanetary disk. Geochimica et Cosmochimica Acta, 168, 151–171.

Goldstein JI, Scott ERD, & Chabot NL (2009). Iron meteorites: Crystallization, thermal history, parent bodies, and origin. Chemie der Erde-Geochemistry, 69(4), 293–325.

Hellmann JL, Kruijer TS, Van Orman JA, Metzler K, & Kleine T (2019). Hf-W chronology of ordinary chondrites. Geochimica et Cosmochimica Acta.

Hilton CD, Bermingham KR, Walker RJ, & McCoy TJ (2019). Genetics, crystallization sequence, and age of the South Byron Trio iron meteorites: New insights to carbonaceous chondrite (CC) type parent bodies. Geochimica et Cosmochimica Acta, 251, 217–228.

Horan MF, Walker RJ, Morgan JW, Grossman JN, Rubin AE (2003) Highly siderophile elements in chondrites. Chem. Geol 196, 5–20.

Jones JH, & Malvin DJ (1990). A nonmetal interaction model for the segregation of trace metals during solidification of Fe-Ni-S, Fe-Ni-P, and Fe-Ni-SP alloys. Metallurgical transactions B, 21(4), 697–706.

Kleine T, Mezger K, Münker C, Palme H, & Bischoff A (2004). 182Hf-182W isotope systematics of chondrites, eucrites, and martian meteorites: Chronology of core formation and early mantle differentiation in Vesta and Mars1. Geochimica et Cosmochimica Acta, 68(13), 2935–2946.

Kruijer TS, Kleine T, Fischer-Gödde M, Burkhardt C, & Wieler R (2014a). Nucleosynthetic W isotope anomalies and the Hf–W chronometry of Ca–Al-rich inclusions. Earth and Planetary Science Letters, 403, 317–327.

Kruijer TS, Touboul M, Fischer-Gödde M, Bermingham KR, Walker RJ, & Kleine T (2014b). Protracted core formation and rapid accretion of protoplanets. Science, 344(6188), 1150–1154. [PubMed: 24904163]

Kruijer TS, Burkhardt C, Budde G, & Kleine T (2017). Age of Jupiter inferred from the distinct genetics and formation times of meteorites. Proceedings of the National Academy of Sciences, 201704461.

Lu Q and Masuda A (1994). The isotopic composition and atomic weight of molybdenum. International Journal of Mass Spectrometry and Ion Processes, 130(1–2), 65–72.

Ludwig KR (2003). Users manual for ISOPLOT/EX, version 3 A geochronological toolkit for Microsoft Excel. Berkeley Geochronology Center Special Publication, (4).

McCoy TJ, Corrigan CM, Nagashima K, Reynolds VS, Ash RD, McDonough WF, Yang J, Goldstein JI, & Hilton CD (2019). The Milton pallasite and South Byron Trio Irons: Evidence for oxidation and core crystallization. Geochimica et Cosmochimica Acta.

McCoy TJ, Walker RJ, Goldstein JI, Yang J, McDonough WF, Rumble D, Chabot NL, Ash RD, Corrigan CM, Michael JR, & Kotula PG (2011). Group IVA irons: New constraints on the crystallization and cooling history of an asteroidal core with a complex history. Geochimica et Cosmochimica Acta, 75(22), 6821–6843.

Nanne JA, Nimmo F, Cuzzi JN, & Kleine T (2019). Origin of the non-carbonaceous–carbonaceous meteorite dichotomy. Earth and Planetary Science Letters, 511, 44–54.

Pernicka E, & Wasson JT (1987). Ru, Re, OS, Pt and Au in iron meteorites. Geochimica et Cosmochimica Acta, 51(6), 1717–1726.

Poole GM, Rehkämper M, Coles BJ, Goldberg T, & Smith CL (2017). Nucleosynthetic molybdenum isotope anomalies in iron meteorites–new evidence for thermal processing of solar nebula material. Earth and Planetary Science Letters, 473, 215–226.

Rehkämper M, & Halliday AN (1997). Development and application of new iondashexchange techniques for the separation of the platinum group and other siderophile elements from geological samples. Talanta, 44(4), 663–672. [PubMed: 18966788]

Rubin AE (2018). Carbonaceous and noncarbonaceous iron meteorites: Differences in chemical, physical, and collective properties. Meteoritics & Planetary Science, 53(11), 2357–2371.

NASA Author Manuscript NASA Author Manuscript NASA Author Manuscript

Rusk B (2009). Laser Ablation ICP-MS in the Earth Sciences: Current Practices and Outstanding Issues. Economic Geology, 104(4), 601–602.

Schaudy R, Watson JT, & Buchwald VF (1972). The chemical classification of iron meteorites. VI. A reinvestigation of irons with Ge concentration lower than 1 ppm. Icarus, 17(1), 174–192.

Scott ER, & Wasson JT (1975). Classification and properties of iron meteorites. Reviews of Geophysics, 13(4), 527–546.

Trinquier A, Birck JL, & Allegre CJ (2007). Widespread 54Cr heterogeneity in the inner solar system. The Astrophysical Journal, 655(2), 1179.

Trinquier A, Elliott T, Ulfbeck D, Coath C, Krot AN, & Bizzarro M (2009). Origin of nucleosynthetic isotope heterogeneity in the solar protoplanetary disk. Science, 324(5925), 374–376. [PubMed: 19372428]

Touboul M, & Walker RJ (2012). High precision tungsten isotope measurement by thermal ionization mass spectrometry. International Journal of Mass Spectrometry, 309, 109–117.

Vockenhuber C, Oberli F, Bichler M, Ahmad I, Quitté G, Meier M, Halliday AN, Lee DC, Kutschera W, Steier P, & Gehrke RJ (2004). New Half-Life Measurement of H f 182: Improved Chronometer for the Early Solar System. Physical Review Letters, 93(17), 172501. [PubMed: 15525068]

Völkening J, Köppe M, & Heumann KG (1991). Tungsten isotope ratio determinations by negative thermal ionization mass spectrometry. International Journal of Mass Spectrometry and Ion Processes, 107(2), 361–368.

Wasson JT (1969). The chemical classification of iron meteorites—III. Hexahedrites and other irons with germanium concentrations between 80 and 200 ppm. Geochimica et Cosmochimica Acta, 33(7), 859–876.

Wasson JT (1999). Trapped melt in IIIAB irons; solid/liquid elemental partitioning during the fractionation of the IIIAB magma. Geochimica et Cosmochimica Acta, 63(18), 2875–2889.

Wasson JT, & Kallemeyn GW (1988). Compositions of chondrites. Philosophical Transactions of the Royal Society of London. Series A, Mathematical and Physical Sciences, 325(1587), 535–544.

Walker RJ, Horan MF, Morgan JW, Becker H, Grossman JN, & Rubin AE (2002). Comparative 187Re-187Os systematics of chondrites: Implications regarding early solar system processes. Geochimica et Cosmochimica Acta, 66(23), 4187–4201.

Walker RJ, McDonough WF, Honesto J, Chabot NL, McCoy TJ, Ash RD, & Bellucci JJ (2008). Modeling fractional crystallization of group IVB iron meteorites. Geochimica et Cosmochimica Acta, 72(8), 2198–2216.

Walker RJ (2012). Evidence for homogeneous distribution of osmium in the protosolar nebula. Earth and Planetary Science Letters, 351, 36–44.meteorites. Geochimica et Cosmochimica Acta, 72(8), 2198–2216.

Warren PH (2011). Stable-isotopic anomalies and the accretionary assemblage of the Earth and Mars: A subordinate role for carbonaceous chondrites. Earth and Planetary Science Letters, 311(1–2), 93–100.

Worsham EA, Walker RJ, & Bermingham KR (2016). High-precision molybdenum isotope analysis by negative thermal ionization mass spectrometry. International Journal of Mass Spectrometry, 407, 51–61. [PubMed: 30842700]

Worsham EA, Bermingham KR, & Walker RJ (2017). Characterizing cosmochemical materials with genetic affinities to the Earth: genetic and chronological diversity within the IAB iron meteorite complex. Earth and Planetary Science Letters, 467, 157–166. [PubMed: 30713346]

Worsham EA, Burkhardt C, Budde G, Fischer-Gödde M, Kruijer TS, & Kleine T (2019). Distinct evolution of the carbonaceous and non-carbonaceous reservoirs: Insights from Ru, Mo, and W isotopes. Earth and Planetary Science Letters, 521, 103–112.

NASA Author Manuscript

NASA Author Manuscript

NASA Author Manuscript

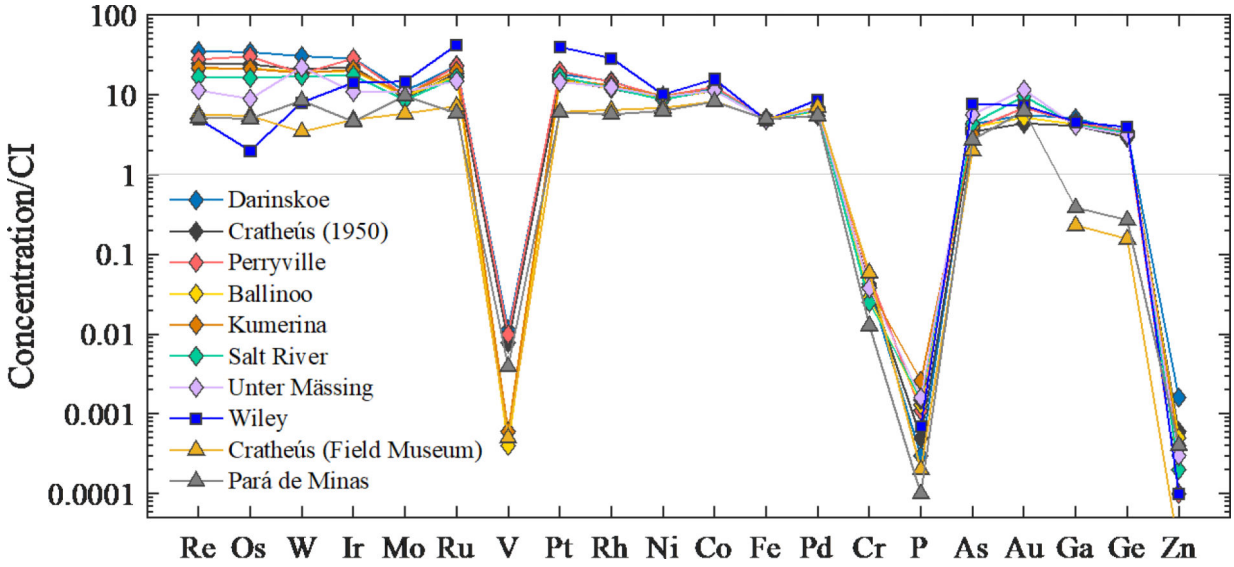

Figure 1.

CI chondrite normalized abundances of siderophile elements for the IIC irons, Wiley and Pará de Minas. Elements are listed in order of decreasing 50% condensation temperatures from left to right. Bulk composition data were normalized to data for CI chondrites (Lodders and Fegley, 1998).

NASA Author Manuscript

NASA Author Manuscript

NASA Author Manuscript

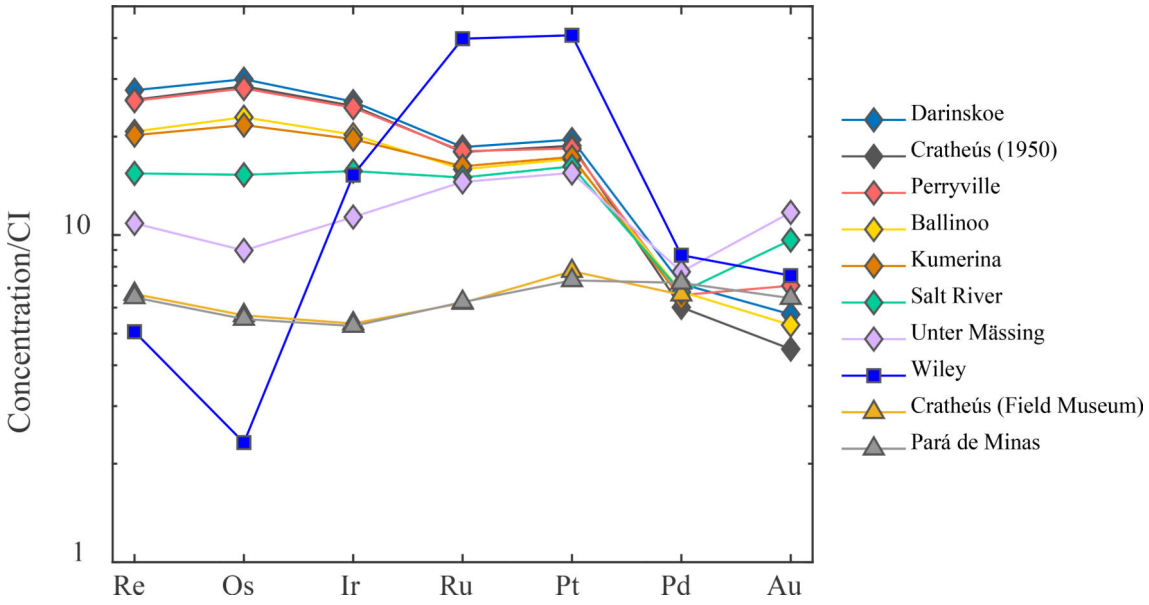

Figure 2.

Bulk CI chondrite normalized abundance plot of HSE abundances. Data for all HSE except Au were obtained by isotope dilution for bulk samples of the IIC irons, Cratheús (Field Museum) and Pará de Minas (IVA iron). The Au data were obtained by laser ablation ICP-MS. The pattern for Wiley is considerably different from the other IIC irons and inconsistent with it being a IIC iron. Bulk composition data were normalized to Re, Os, Ir, Ru, Pt and Pd concentrations for the CI chondrite Orgueil reported by Horan et al. (2003) and Au data were normalized to average Au concentrations of CI chondrites reported by Fischer-Gödde et al. (2010).

NASA Author Manuscript

NASA Author Manuscript

NASA Author Manuscript

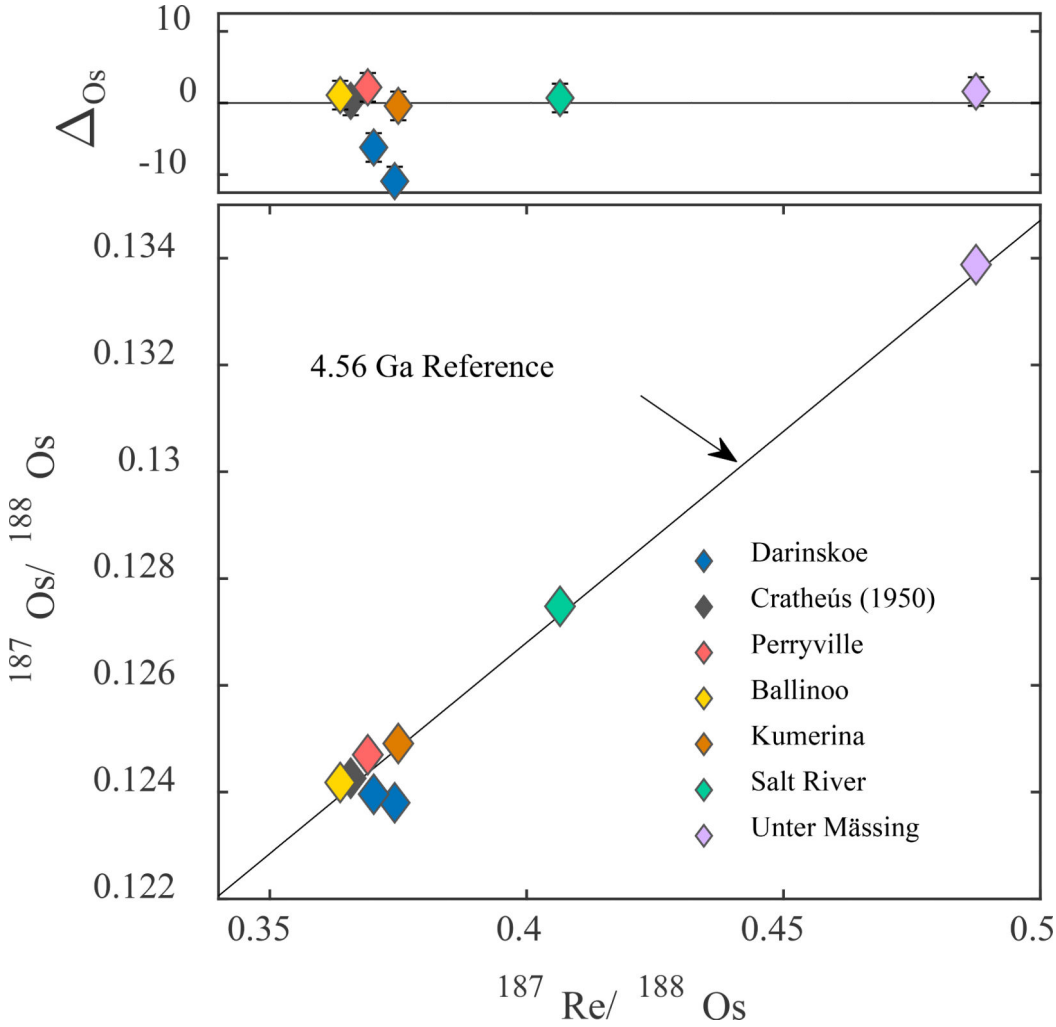

Figure 3.

$^{187}Re/^{188}Os$ versus $^{187}Os/^{188}Os$ isochron diagram for group IIC iron meteorites. Symbols in lower figure are larger than error bars. Upper figure shows $^{187}Re/^{188}Os$ versus Δ values (parts per 10,000 deviation from the IIC isochron). The error bars represent the total analytical uncertainties (2σ). Data are shown relative to a 4.56 Ga reference isochron.

NASA Author Manuscript

NASA Author Manuscript

NASA Author Manuscript

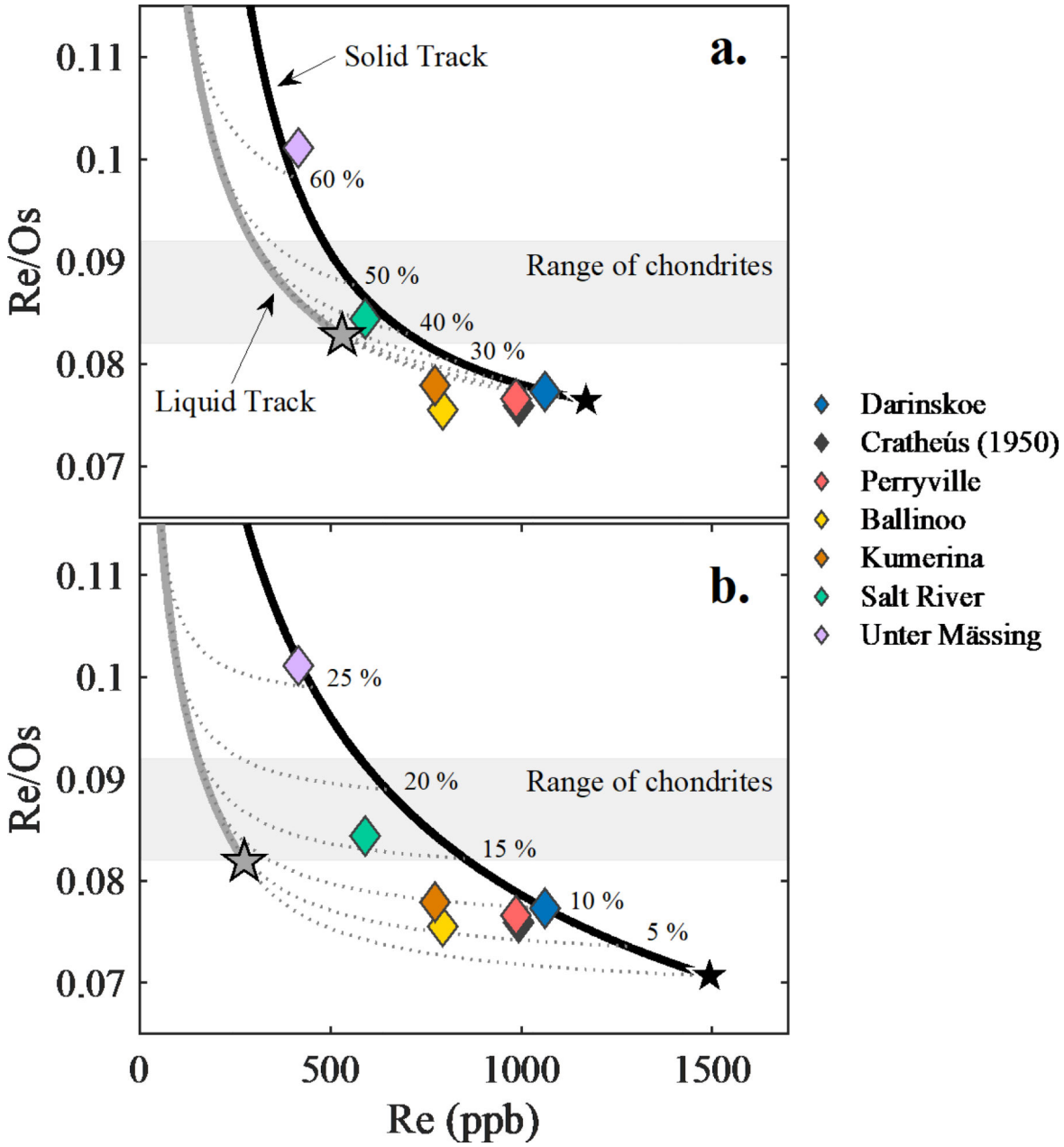

Figure 4a-b.

(a) Fractional crystallization model for Re (ppb) versus Re/Os calculated for initial S and P concentrations of 0 and 3 wt.%, respectively. The dashed grey lines show mixing curves connecting the equilibrium solid and liquid tracks at 10% increments. **(b)** Fractional crystallization model for Re (ppb) versus Re/Os calculated for initial S and P concentrations of 8 and 2 wt.%, respectively. The dashed grey lines show mixing curves connecting the equilibrium solid and liquid tracks at 5% increments. The black line represents the solid track and the grey line represents the liquid track. The colored diamonds are the data for the IIC irons. The grey area is the range for bulk chondrites (Walker et al., 2002). The black and grey stars represent the first solid and liquid composition to form, respectively.

NASA Author Manuscript

NASA Author Manuscript

NASA Author Manuscript

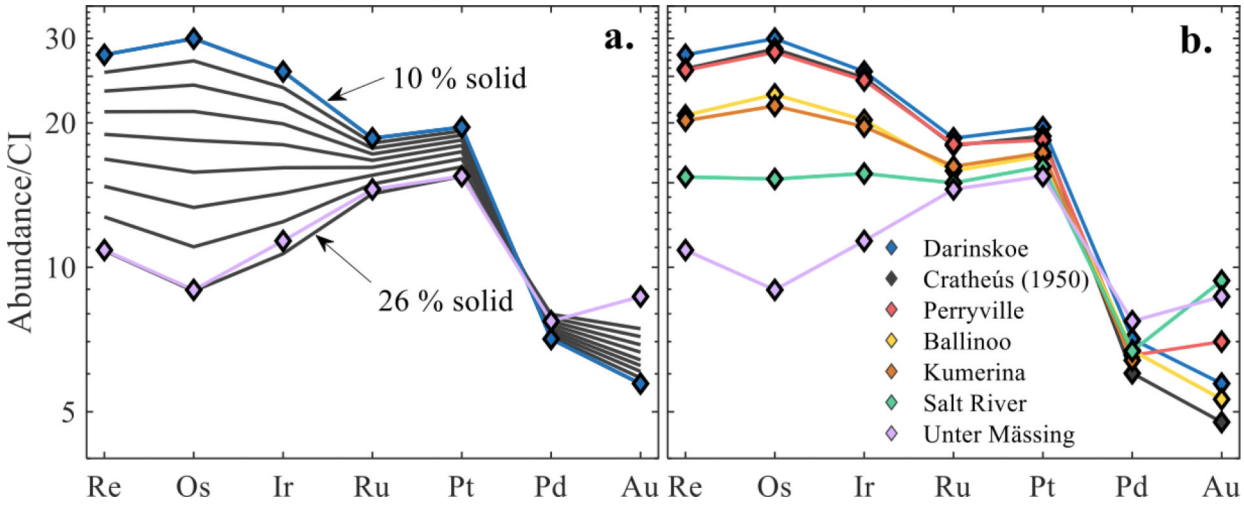

Figure 5.

(a) CI chondrite normalized solid compositions calculated using the preferred fractional crystallization model at 2 wt.% increments. The modeled results are in good agreement with the observed patterns for the IIC irons **(b)**.

NASA Author Manuscript

NASA Author Manuscript

NASA Author Manuscript

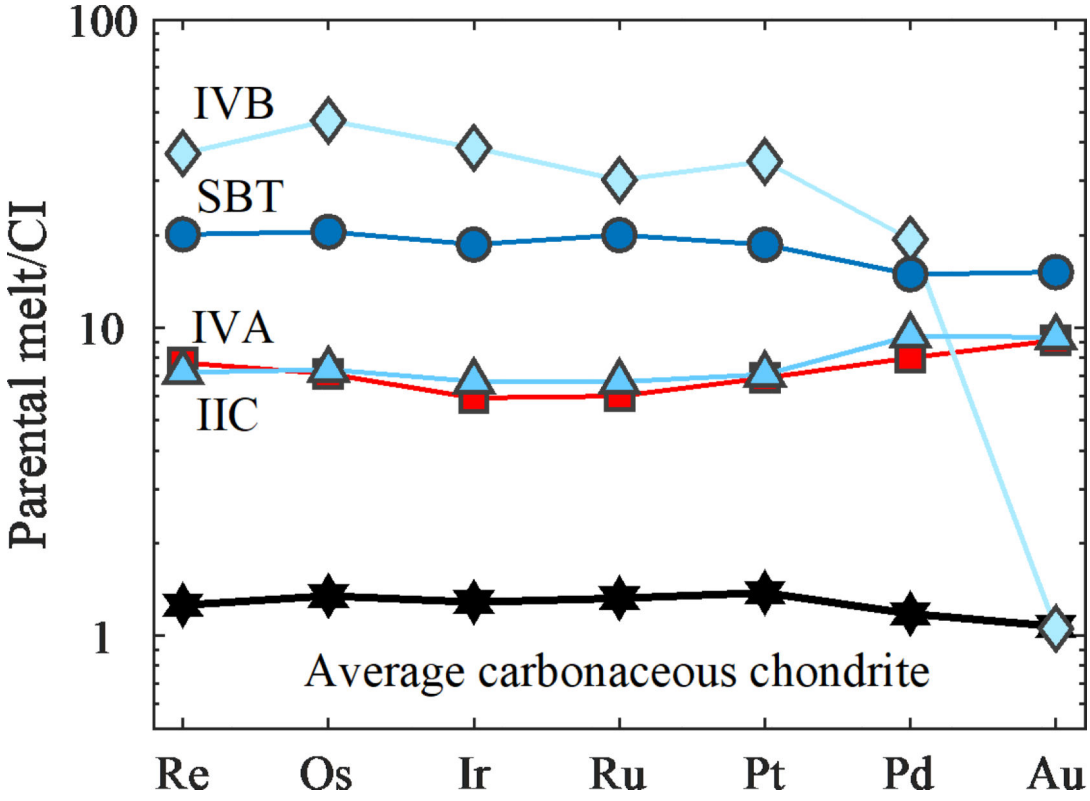

Figure 6.

Plot of calculated parental melt HSE concentrations, normalized to Re, Os, Ir, Ru, Pt and Pd concentrations for the CI chondrite Orgueil reported by Horan et al. (2003) and Au data were normalized to average Au concentrations of CI chondrites reported by Fischer-Gödde et al. (2010). Parameter concentrations are plotted from Table 6. For comparison, the initial parental melt concentrations estimated by Walker et al., 2008 (IVB), McCoy et al., 2011 (IVA), and Hilton et al., 2019 (SBT) are shown.

NASA Author Manuscript

NASA Author Manuscript

NASA Author Manuscript

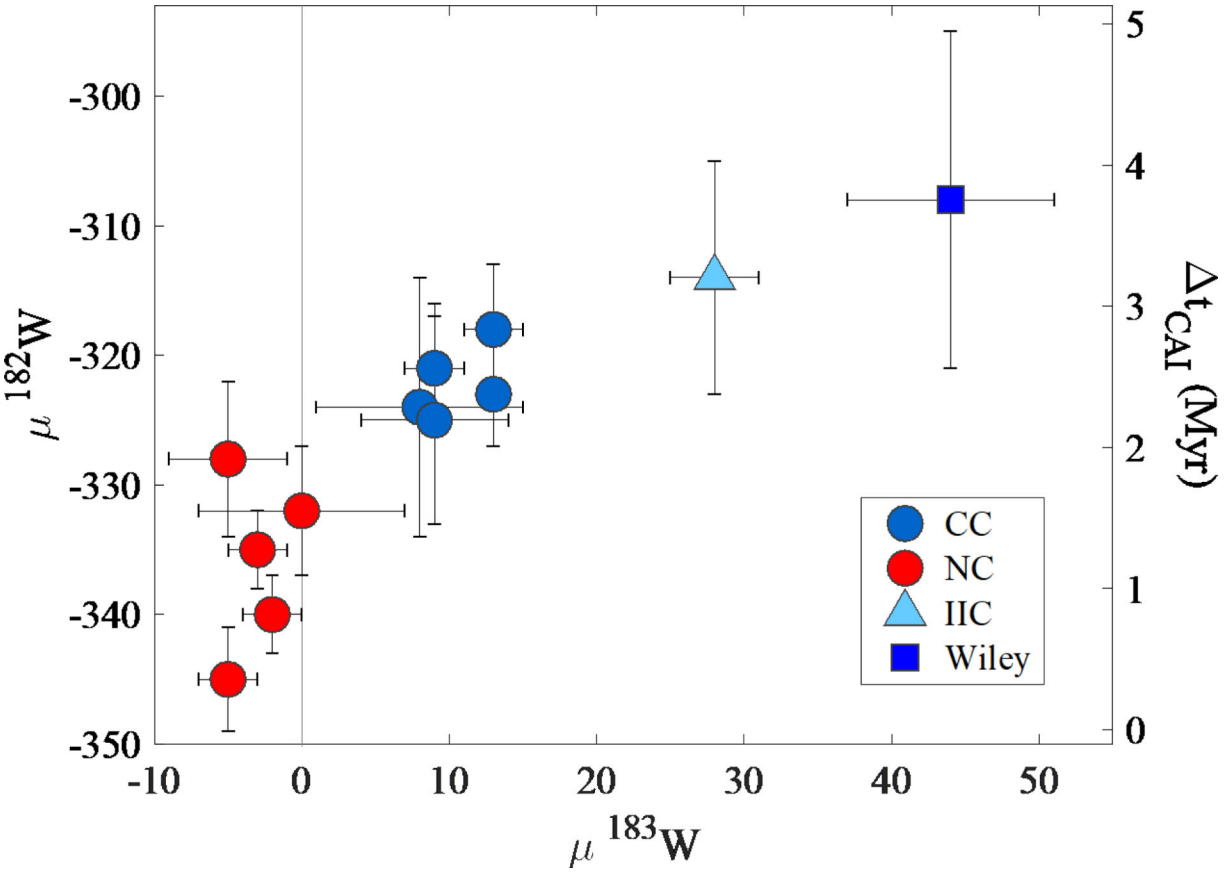

Figure 7.

Plot of μ^{183}W versus μ^{182}W of magmatic iron meteorites. NC type meteorites include group averages of data for IC, IIAB, IIIAB IIIE and IVA irons. CC type meteorites include group averages for IID, IIF, IIIF, IVB, South Byron Trio (SBT), IIC and ungrouped iron, Wiley. Data are from this study, Kruijer et al. (2017), and Hilton et al. (2019).

NASA Author Manuscript

NASA Author Manuscript

NASA Author Manuscript

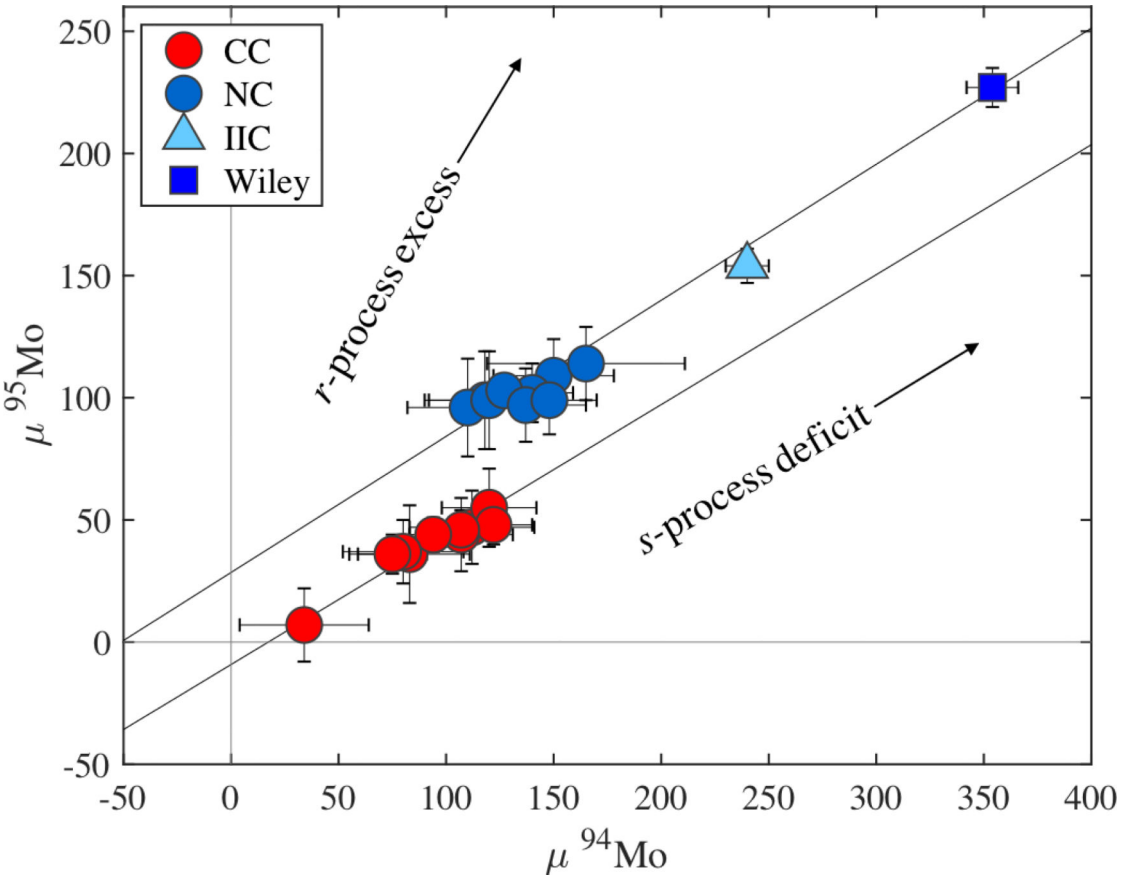

Figure 8.

Plot of μ^{94}Mo versus μ^{95}Mo for iron meteorites using data from Table 4 and group averages reported by Bermingham et al. (2018), Worsham et al. (2019) and Hilton et al. (2019). NC type meteorites include group averages of IC, IIAB, IIIAB, IIIE, IVA and one ungrouped iron, Gebel Kamil. CC type meteorites include group averages of IID, IIF, IIIF, IVB, SBT, IIC and four ungrouped irons Wiley, Chinga, Dronino, and Tishomingo. The black lines are linear regressions calculated using *ISOPLOT*.

NASA Author Manuscript

NASA Author Manuscript

NASA Author Manuscript

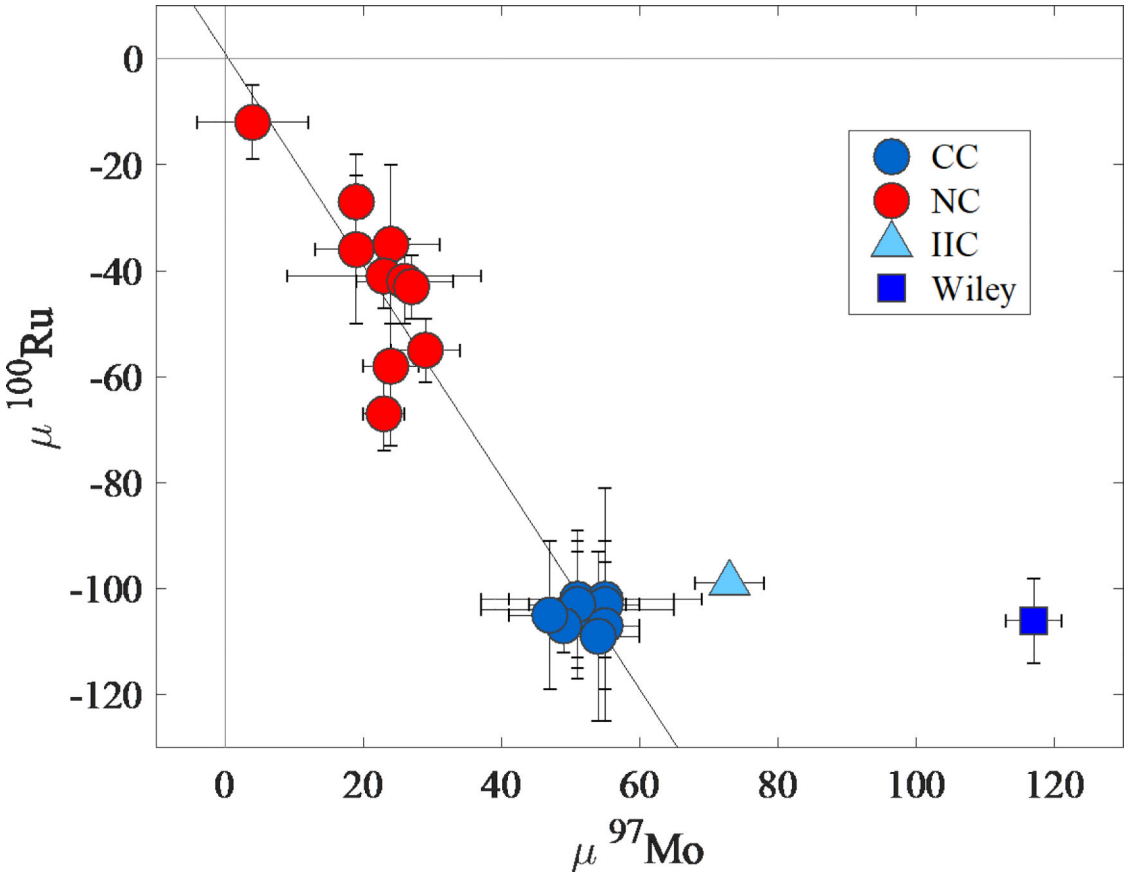

Figure 9.

Plot of μ^{97}Mo versus μ^{100}Ru using data from Table 4 and group averages reported by Bermingham et al. (2018), Worsham et al. (2019) and Hilton et al. (2019). NC type meteorites include group averages of IC, IIAB, IIIAB, IIIE, IVA and one ungrouped iron, Gebel Kamil. CC type meteorites include group averages of IID, IIF, IIIF, IVB, SBT, IIC and four ungrouped irons Wiley, Chinga, Dronino, and Tishomingo. The black line is a linear regressions calculated using *ISOPLOT*.

NASA Author Manuscript

NASA Author Manuscript

NASA Author Manuscript

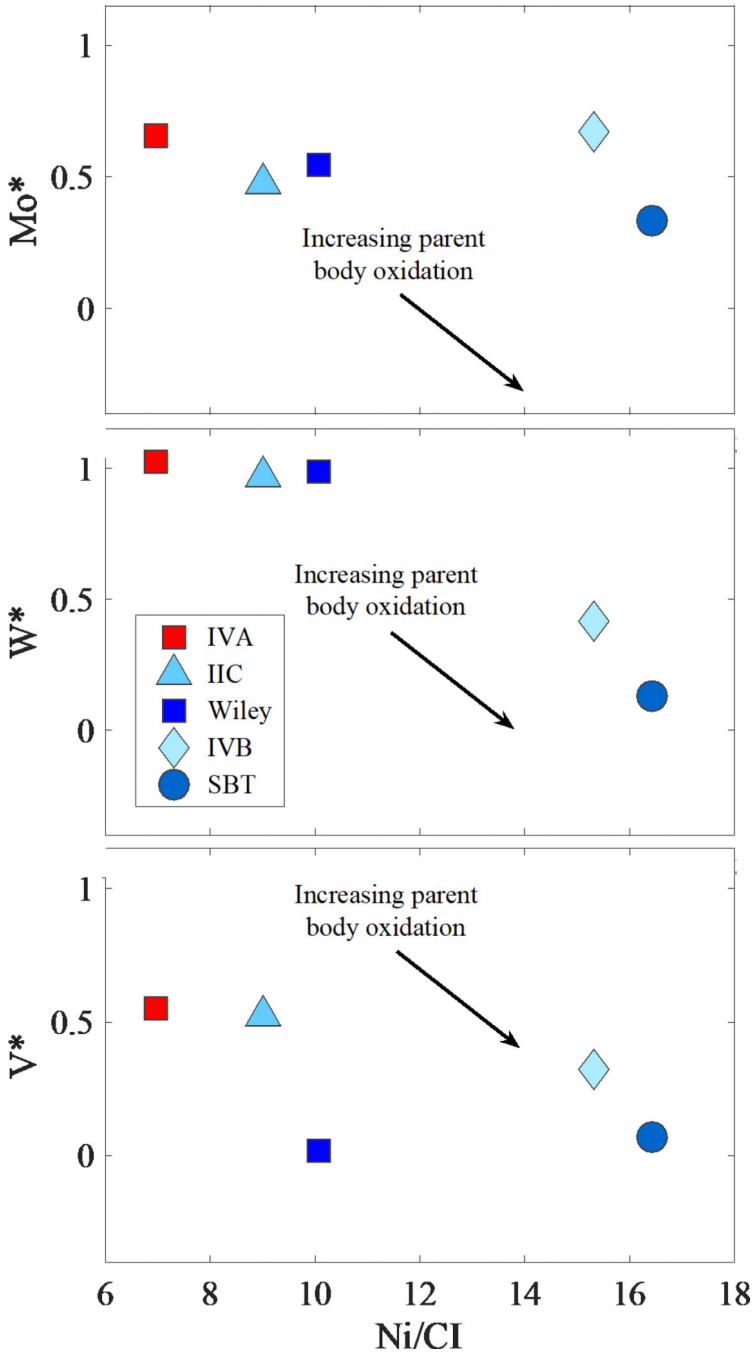

Figure 10.

(a-c) Plot of relative depletions of Ni (CI-normalized) versus Mo, W and V calculated using Eq. 2 for the least evolved irons of the IVB, SBT, IIC and IVA groups and Wiley (Walker et al., 2008; Hilton et al., 2019; McCoy et al., 2011). Blue symbols are the CC bodies and red symbols are the NC bodies. The arrow is the direction that the composition of the parent body will progress with increasing oxidation. Data for the IIC and IVA (NC) group irons generally indicate a less oxidized parent body than the other CC type irons.

NASA Author Manuscript NASA Author Manuscript NASA Author Manuscript

Table 1.

Average elemental concentrations obtained by LA-ICP-MS. Group IIC irons are listed from left to right in order of decreasing Re concentration.

	Darinskoe	Perryville	Cratheús (1950)	Kumerina	Ballinoo	Salt River	Unter Mässing	Wiley	Cratheús (Field Museum)	Parà de Minas
Re	1.4 ± 1.0	1.1 ± 0.3	1.0 ± 0.2	0.9 ± 0.2	0.8 ± 0.2	0.7 ± 0.1	0.4 ± 0.1	0.2 ± 0.1	0.22 ± 0.03	0.21 ± 0.09
Os	17.4 ± 7.2	15.3 ± 2.9	12.2 ± 1.4	10.8 ± 2.3	10.9 ± 1.9	8.2 ± 1.3	4.5 ± 1.3	1.0 ± 0.2	2.8 ± 0.8	2.5 ± 0.3
W	2.8 ± 1.3	1.7 ± 1.5	1.9 ± 0.3	1.7 ± 1.5	1.7 ± 1.2	1.5 ± 1.1	2.0 ± 0.9	0.7 ± 0.5	0.3 ± 0.1	0.8 ± 0.9
Ir	13.7 ± 4.6	13.7 ± 3.0	10.7 ± 1.3	9.9 ± 1.7	9.6 ± 1.0	8.4 ± 0.6	5.2 ± 1.3	6.8 ± 1.0	2.3 ± 0.4	2.2 ± 0.4
Mo	10.3 ± 4.0	9.0 ± 4.4	8.5 ± 4.8	9.3 ± 2.4	8.9 ± 4.3	8.0 ± 2.7	10.1 ± 9.6	13.6 ± 6.2	5.4 ± 0.4	9.0 ± 17.0
Ru	15.9 ± 8.3	15.7 ± 5.7	12.5 ± 1.7	13.6 ± 1.3	11.8 ± 2.4	11.3 ± 0.9	10.2 ± 2.3	28.9 ± 10.8	4.9 ± 0.4	4.0 ± 0.4
V	0.6 ± 0.3	b.d.	0.4 ± 0.9	0.03 ± 0.01	0.02 ± 0.02	b.d.	b.d.	b.d.	0.028 ± 0.001	0.2 ± 0.7
Pt	17.8 ± 5.8	19.5 ± 3.7	15.0 ± 2.4	15.7 ± 2.2	14.8 ± 1.4	16.7 ± 1.9	14.2 ± 5.4	38.9 ± 6.0	6.0 ± 0.8	5.9 ± 0.5
Rh	2.1 ± 0.8	2.0 ± 0.7	1.7 ± 0.2	1.8 ± 0.2	1.7 ± 0.2	1.7 ± 0.1	1.7 ± 0.5	4.0 ± 1.1	0.9 ± 0.3	0.8 ± 0.1
Ni	9.7 ± 3.0	10.4 ± 3.1	9.4 ± 2.3	10.5 ± 2.4	9.5 ± 1.9	9.3 ± 0.4	10.2 ± 3.9	10.8 ± 2.5	7.4 ± 0.3	6.8 ± 1.2
Co	0.6 ± 0.1	0.6 ± 0.1	0.57 ± 0.02	0.58 ± 0.02	0.57 ± 0.05	0.59 ± 0.04	0.57 ± 0.03	0.8 ± 0.1	0.42 ± 0.01	0.41 ± 0.02
Fe[a]	89.0	93.7	91.0	90.3	90.4	90.0	90.2	88.5	91.0	91.5
Pd	3.8 ± 1.4	3.9 ± 1.4	3.0 ± 0.4	3.9 ± 0.9	3.5 ± 0.9	3.5 ± 0.6	3.7 ± 1.1	4.8 ± 1.9	3.9 ± 0.5	3.0 ± 0.9
Cr	103 ± 56	143 ± 96	111 ± 145	101 ± 35	78 ± 51	66 ± 33	100 ± 47	b.d.	155 ± 5	34 ± 59
P	0.3 ± 0.4	1.0 ± 1.2	0.5 ± 0.8	2.4 ± 4.5	1.2 ± 2.1	1.4 ± 2.2	1.5 ± 3.2	0.6 ± 1.0	0.19 ± 0.02	0.06 ± 0.03
Mn	b.d.	b.d.	12.1 ± 22.2	b.d.	b.d.	b.d.	b.d.	b.d.	b.d.	1.0 ± 1.1
As	7.7 ± 2.5	6.7 ± 2.3	6.2 ± 1.0	5.8 ± 0.3	7.1 ± 2.3	7.9 ± 2.9	10.2 ± 2.7	13.9 ± 3.4	3.6 ± 0.5	4.9 ± 2.6
Au	0.8 ± 0.2	1.0 ± 0.1	0.6 ± 0.1	b.d.	0.8 ± 0.0	1.4 ± 0.2	1.3 ± 1.0	1.1 ± 0.1	b.d.	0.9 ± 0.1
Ga	49 ± 10	44 ± 12	40 ± 5	42 ± 4	41 ± 5	41 ± 4	40 ± 6	45 ± 2	2.2 ± 0.3	3.7 ± 3.2
Ge	112 ± 36	113 ± 42	96 ± 11	108 ± 11	101 ± 13	109 ± 13	103 ± 9	129 ± 10	b.d.	b.d.
Zn	0.5 ± 1.6	0.04 ± 0.10	0.2 ± 0.4	0.1 ± 0.2	0.2 ± 0.3	0.1 ± 0.1	0.1 ± 0.1	0.02 ± 0.01	0.008 ± 0.004	0.1 ± 0.2
n	*5*	*6*	*8*	*6*	*7*	*6*	*13*	*6*	*6*	*4*

Nickel, Co, and Fe concentrations reported in wt.%, all others reported in ppm.

The 2σ values reported were determined from the reproducibility of the number of lines measured (*n*) for each sample.

b.d. Concentration data below detection limits.

[a]Fe data were used as an internal standard.

NASA Author Manuscript NASA Author Manuscript NASA Author Manuscript

Table 2.

Osmium isotopic and HSE composition data, obtained by isotope dilution, for IIC irons, Wiley, Cratheús (1931) and Pará de Minas.

Sample	Wt.	Re	Os	Ir	Ru	Pt	Pd	$^{187}Os/^{188}Os$	2σ	$^{187}Re/^{188}Os$	2σ	Δ_{Os}	2 σ
Darinskoe	0.037	1072	13790	11970	12090	16910	3893	0.12380	0.00010	0.3743	0.0004	−9.9	2.0
Duplicate	0.037	1051	13680	11340	12050	16740	4090	0.12396	0.00010	0.3702	0.0004	−5.2	2.0
Cratheús (1950)	0.054	992.6	13070	11310	11650	16110	3385	0.12426	0.00010	0.3658	0.0004	1.3	2.0
Perryville	0.091	985.6	12860	11170	11730	15810	3689	0.12470	0.00010	0.3691	0.0004	3.2	2.0
Ballinoo	0.130	793.7	10510	9234	10320	14670	3778	0.12418	0.00010	0.3637	0.0004	2.1	2.0
Kumerina	0.034	774.2	9945	8947	10540	14880	3603	0.12491	0.00010	0.3750	0.0004	0.3	2.0
Salt River	0.076	590.9	7005	7143	9740	13930	3765	0.12748	0.00010	0.4065	0.0004	1.7	2.0
Unter Mässing	0.072	415.9	4114	5170	9440	13300	4347	0.13388	0.00010	0.4875	0.0004	2.6	2.0
Wiley	0.092	194.3	1064	6949	25870	35050	4884	0.16504	0.00010	0.8845	0.0004	4.5	2.0
Cratheús (Field Museum)	0.088	252.7	2606	2444	4026	6664	3699	0.13229	0.00010	0.4676	0.0004	2.2	2.0
Pará de Minas	0.059	247.4	2540	2402	4052	6245	4021	0.13227	0.00010	0.4696	0.0004	0.5	2.0

Samples are in order of decreasing Re concentration.

Unit of weight are in g. All other concentrations are in ppb.

The uncertainties for Re and Os concentrations are ± 0.1% and the uncertainties for Ir, Ru, Pt and Pd concentrations are <2%.

Δ_{Os} is calculated by $\Delta_{Os} = 10^4 (^{187}Os/^{188}Os_{IIC} - (0.0956 + 0.078 \times {}^{187}Re/^{188}Os_{IIC}))$, where 0.0956 is the IIC initial $^{187}Os/^{188}Os$ and 0.078 is the slope of the IIC isochron.

NASA Author Manuscript

NASA Author Manuscript

NASA Author Manuscript

Table 3.

Osmium isotopic compositions of select IIC irons and Wiley.

Sample	n	μ^{189}Os	2σ	μ^{190}Os	2σ
Ballinoo	2	+3	8	−4	18
Darinskoe	2	−5	7	0	10
Perryville	3	+5	5	0	18
Wiley	3	+2	5	−1	5

n - number of analyses for each meteorite sample. The reported values are the average for each meteorite sample. Uncertainties represent the largest 2SD of the standards run during an analytical campaign.

NASA Author Manuscript

NASA Author Manuscript

NASA Author Manuscript

Table 4.

Molybdenum and Ru isotopic compositions for IIC irons and Wiley.

Sample	n	μ^{92}Mo	2σ	μ^{94}Mo	2σ	μ^{95}Mo	2σ	μ^{97}Mo	2σ	n	μ^{100}Ru	2σ
Ballinoo	1	372	34	252	16	159	7	70	8	2	−99	4
Darinskoe	2	351	47	235	30	149	19	75	10	2	−100	6
Perryville	2	345	66	239	21	147	15	72	19	1	−100	6
IIC Average	5	353	21	240	10	150	7	73	5	5	−99	2
Wiley	10	467	32	354	12	227	8	117	4	4	−106	8

n - number of analyses of multiple loads onto different filaments of material from the same chemistry. The reported values are the averages for each sample. Uncertainties are 2SD ($n < 4$) or 2SE ($n \geq 4$).

NASA Author Manuscript

NASA Author Manuscript

NASA Author Manuscript

Table 5.

Tungsten isotopic compositions for IIC irons and Wiley.

Sample	n	$\mu^{182}W_{Measured}$	2σ	$\mu^{183}W_{Measured}$	2σ	$\mu^{182}W_{Corrected}$	2σ	ΔT_{CAI}	2σ
Ballinoo	1	−265	10	+34	6	−313	13	3.3	1.4
Perryville	4	−277	8	+27	1	−314	4	3.2	0.6
IIC Average	5	−274	8	+28	3	−314	9	3.2	0.7
Wiley	1	−246	8	+44	7	−308	13	3.8	1.4

n - number of analyses for each meteorite sample. The reported values are the averages for each sample. Uncertainties are the 2SD (n < 4) of the standards run during an analytical campaign or 2SE (n ≥ 4) of the sample values. The $\mu^{182}W$ values are corrected for the *r*- process excess of ^{183}W.

NASA Author Manuscript

NASA Author Manuscript

NASA Author Manuscript

Table 6.

Calculated initial concentrations of HSE (in ppb) for the parameters discussed in the text.

	Re	Os	Ir	Ru	Pt	Pd	Au
IIC	280	3350	3050	4340	6070	5300	1350
IVB[a]	2800	37000	27000	27400	29500	8600	150
IVA[b]	295	3250	2700	3900	5900	4500	1320
SBT[c]	770	9400	8500	13000	16000	8400	2200[d]

[a]Data from Walker et al. (2008)

[b]Data from McCoy et al. (2011)

[c]Data from Hilton et al. (2019), SBT – South Byron Trio

[d]Data from McCoy et al. (2019).